

ULTRAFAST PHOTOCARRIER RELAXATION MECHANISMS IN SPUTTER-
DEPOSITED CDTE QUANTUM DOT THIN FILMS

by

Christophe Rene Henri Juncker

A Dissertation Submitted to the Faculty of the
DEPARTMENT OF MATERIALS SCIENCE AND ENGINEERING

In Partial Fulfillment of the Requirements
For the Degree of

DOCTOR OF PHILOSOPHY

In the Graduate College
THE UNIVERSITY OF ARIZONA

2007

THE UNIVERSITY OF ARIZONA
GRADUATE COLLEGE

As members of the Dissertation Committee, we certify that we have read the dissertation prepared by Christophe Rene Henri Juncker entitled Ultrafast Photocarrier Relaxation Mechanisms in Sputter-Deposited CdTe Quantum Dot Thin Films and recommend that it be accepted as fulfilling the dissertation requirement for the Degree of Doctor of Philosophy

_____ Date: 09/10/07
Joseph H. Simmons

_____ Date: 09/10/07
Barrett G. Potter

_____ Date: 09/10/07
Pierre Lucas

_____ Date: 09/10/07
Nasser Peyghambarian

_____ Date: 09/10/07
Neal Armstrong

Final approval and acceptance of this dissertation is contingent upon the candidate's submission of the final copies of the dissertation to the Graduate College.

I hereby certify that I have read this dissertation prepared under my direction and recommend that it be accepted as fulfilling the dissertation requirement.

_____ Date: 09/10/07
Dissertation Director: Joseph Simmons

STATEMENT BY AUTHOR

This dissertation has been submitted in partial fulfillment of requirements for an advanced degree at the University of Arizona and is deposited in the University Library to be made available to borrowers under rules of the Library.

Brief quotations from this dissertation are allowable without special permission, provided that accurate acknowledgment of source is made. Requests for permission for extended quotation from or reproduction of this manuscript in whole or in part may be granted by the head of the major department or the Dean of the Graduate College when in his or her judgment the proposed use of the material is in the interests of scholarship. In all other instances, however, permission must be obtained from the author.

SIGNED: Christophe Rene Henri Juncker

ACKNOWLEDGEMENTS

I would like to thank my advisor, Dr Simmons, for his guidance during my time in graduate school. I had the opportunity to learn from many members of the faculty of the Department of Materials Science and Engineering at the University of Arizona. They include Dr Pierre Lucas, Dr B.G. Potter, Dr Pierre Deymier and Dr Srinu Raghavan. Finally, I could not have completed this work without the support of Denisse, my parents, Jacqueline and Michel, and my sister, Laurence.

TABLE OF CONTENTS

LIST OF FIGURES.....	8
LIST OF TABLES.....	10
ABSTRACT	11
CHAPTER 1 MOTIVATION.....	12
1.1 Overview.....	12
1.2. Applications for quantum dots.....	13
1.3 Statement of the problem.....	14
CHAPTER 2 BACKGROUND	16
2.1 Structure and properties of bulk Cadmium Telluride	16
2.1.1 Crystal structure of Cadmium Telluride	16
2.1.2. Electronic band structure	18
2.2 Effects of confinement on the band structure	24

TABLE OF CONTENTS - *Continued*

2.3 Excitonic effects in the strong confinement regime	29
2.4 Role of traps and surface states.....	32
2.5 Phonon effects.....	34
2.6 Auger effects.....	35
CHAPTER 3 EXPERIMENTAL TECHNIQUES	38
3.1 Sample fabrication	38
3.2 Sample characterization	40
3.2.1 Transmission spectroscopy	40
3.2.2 Photoluminescence measurements.....	43
3.3 Ultrafast measurements	45
3.3.1 Laser system description	45
3.3.2 Pump-probe apparatus description.....	52
3.3.3 Experimental procedure.....	55
CHAPTER 4 RESULTS AND DISCUSSION	58

TABLE OF CONTENTS - *Continued*

4.1 Transmission spectroscopy.....	58
4.1.1 Calculation of the absorption coefficient of the film.....	58
4.1.2 Absorption spectrum analysis.....	63
4.2 Photoluminescence.....	68
4.3 Ultrafast measurements.....	72
4.3.1 Three-level model.....	72
4.3.2 Considerations about Auger effects.....	75
CHAPTER 5 CONCLUSION.....	82
REFERENCES.....	87

LIST OF FIGURES

Figure 1: Dependence of the density of states on the dimensionality of semiconductors.	13
Figure 2: a) Zincblende crystal structure, b) Bravais lattice of the zincblende structure .	17
Figure 3: Phonon dispersion curve for CdTe.....	17
Figure 4: Energy dispersion curves for (a) typical bulk direct-gap semiconductor, (b) exciton in bulk crystal.....	22
Figure 5: Band structure of bulk Cadmium Telluride.....	23
Figure 6: Bandstructure of CdTe quantum dots calculated in the 8 parabolic band model	28
Figure 7: Size dependence of the exciton sublevels	32
Figure 8: Auger autoionization mechanism.....	37
Figure 9: Interference on a thin film deposited on a substrate	41
Figure 10: Laser system.....	45
Figure 12: Normalized transmittance of the four samples about the visible.	60
Figure 13: Normalized transmittance of the four samples in the near infrared.	60
Figure 14: Examples of fitting x and d to the data (a) in the NIR, low absorption region and, (b) in the visible region, using second derivatives.....	61
Figure 15: Calculated absorption coefficients of the four films around the visible region.	62

LIST OF FIGURES - *Continued*

Figure 16: Calculated absorption coefficient derivatives of the four films around the visible region.....	62
Figure 17: Energy levels.	66
Figure 18: First derivative and absorption coefficient curve fittings for each sample	67
Figure 19: Normalized photoluminescence spectra.....	68
Figure 20: Compared absorption coefficient spectra, contributions of the first transition to the absorption coefficient, and photoluminescence spectra.....	71
Figure 21: (a) energy diagram for the three-level model; (b) decay scheme for quantized Auger relaxation.....	77
Figure 22: Differential transmission results and curve fits as a function of delay.	79
Figure 23: Dot radius dependence of x compared to normalized $1/a$ and $1/a^3$	80
Figure 24: Initial population of 1-pair states, 2-pair states, ..., 8-pair states as a function of the average number of e-h pairs per quantum dot.	81

LIST OF TABLES

Table 1: Heat treatment of the various samples.....	39
Table 2: Optical properties of the CdTe samples.....	71
Table 3: Fittig parameters for the three-level model.	80

ABSTRACT

Photocarrier relaxation mechanisms in CdTe quantum dots in the strong confinement regime were investigated using femtosecond pump-probe measurements. The quantum dots were formed in films deposited on silica substrates using a sequential RF magnetron sputtering process with heat treatment to grow crystallites of various sizes. Size selection was achieved by tuning the laser to various wavelengths across the first excitation transition. The recombination mechanism showed a biexponential decay, which was fitted to a three-level model. It was shown that recombination occurs increasingly through the intermediate energy level as the size of the dots decreases. The nature of the intermediate level and the role of Auger recombination is discussed.

CHAPTER 1

MOTIVATION

1.1 Overview

Probably the most important reason for the popularity of nanotechnology is the range of new properties seen in materials when their dimensions are much smaller than the bulk. Indeed, nanomaterials are defined by convention as materials on the length scale of 1 to 100 nm.[1] This definition means that such nanomaterials covers a range between single atoms or molecules and bulk materials, that is, clusters of a finite number of atoms. Moreover, their properties often strongly depend on size, allowing scientists and engineers to carefully tailor them to their needs. Popular fabrication methods include phase separation techniques in glass, wet chemical synthesis, or deposition techniques such as sputtering, molecular beam epitaxy, chemical vapor deposition, or pulsed laser deposition. Investigation of nanostructures is made possible by powerful microscopic techniques with resolutions of a few Angstroms such as scanning tunneling microscopy, transmission electron microscopy, atomic force microscopy, and near-field scanning optical microscopy.

Loss of dimensionality in semiconductors, that is, increasing the number of directions in which the carriers are confined, has a strong impact on the band structure in particular. While in the non-confined directions, the carriers behave as free particles and have quasi-continuous energy bands, in each direction of confinement, they behave as

“particles-in-a-box”, and their energy bands in these directions become discrete. The smaller the particle, the larger the energy separating the confined levels. This explains the difference illustrated in figure 1 in the density of states between bulk, quantum wells, quantum wires and quantum dots. Confinement in all three directions for a single quantum dot results in discrete absorption levels centered on size-dependent energies. Moreover, the confinement increases nonlinearities in quantum dots.[2]

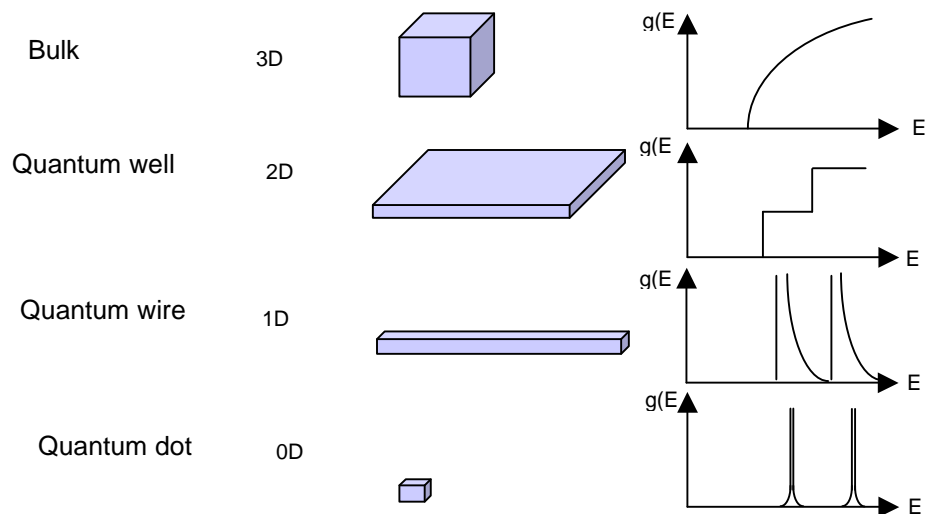


Figure 1: Dependence of the density of states on the dimensionality of semiconductors. After [3]

1.2. Applications for quantum dots

The tunability of the bandgap of quantum dots finds applications in various fields. First, their high photoluminescence quantum yield and low photobleaching make them ideal candidates for fluorescent biomarkers over organic compounds,[4] and much research has been invested in developing adequate surface ligands. Second, the

conversion efficiency of silicon solar cells is limited in part by its bandgap. Photons with energy smaller than the bandgap cannot be absorbed. Therefore, a large part of the spectrum, that is, in the near infrared to mid infrared, does not contribute to electricity generation. Simply increasing the bandgap does not necessarily increase conversion efficiency. Rather, a distribution of energy gaps can maximize conversion efficiencies. Multijunctions have been created, but their cost is high. Quantum dots, with their tunable bandgaps, offer an interesting alternative.[3]

Quantum dot lasers have also been demonstrated in epitaxial III-V materials.[5] Experimental observation of gain in smaller, chemically synthesized II-VI quantum dots [6] and in QD in glass matrix [7] show that II-VI QD lasers are feasible. Lasing is attributed to the splitting of the lowest electron-hole pair state into an absorbing and emitting state.[6] A competing model attributes lasing to the transition between 2 electron-hole pair states and 1 electron-hole pair states.[8] Such QD lasers, if successively tuned to wavelengths about 1.3 and 1.5 μm , could find applications in the telecommunication industry.[9] CdTe quantum dots could also find applications in ultrafast optical switching[10, 11] due to their sub-picosecond response time and high nonlinearities.[12, 13]

1.3 Statement of the problem

The characterization of carrier dynamics in quantum dots is important to understand their structures and optical properties. For example, understanding carrier

dynamics is a first step towards building a gain medium for a laser. Three main approaches exist for the fabrication of quantum dot nanocomposites : wet, or colloidal chemistry, semiconductor-doped glass, (SDG) and sputter deposition. The wet chemistry approach seems in many ways the best approach, since it offers great control over the size dispersion of the dots and over their surface. However, this approach seems impractical for solid-state devices. The SDG approach tends to create deep traps due to impurities, and size dispersion is important due to thermal annealing. Sputter deposition has the same issues concerning size dispersions as the glass approach. The technique also offers little control over the surface, but has the inherent advantage of being solid state. Furthermore, since this technique consists in depositing thin films, it offers the possibility for the creation of waveguides. Therefore, we propose to study the carrier dynamics of sputter-deposited CdTe quantum dots as a function of their size.

CHAPTER 2

BACKGROUND

2.1 Structure and properties of bulk Cadmium Telluride

2.1.1 Crystal structure of Cadmium Telluride

Reference [14] lists valuable structural data and properties of semiconductors. Cadmium Telluride is a II-VI semiconductor. Bonds between Cd and Te atoms are mostly covalent with about 4 percent ionicity. Hybridization of the $5s^2$ orbital of Cd and $5s^2p^4$ of Te forms 4 equivalent sp^3 orbitals for both Cd and Te. Thus, the CdTe has the zincblende crystal structure at room temperature and under atmospheric pressure.[14] One species occupies a face-centered cubic configuration, while the other one occupies half of the tetrahedral sites, forming itself a face centered cubic lattice. The resulting configuration, shown in figure 2 along with the corresponding Bravais lattice, is therefore similar to silicon's diamond structure. The lattice constant at 300 K has been reported around 6.482 \AA [15] to 6.486 \AA [16]. It should be noted that its phase changes to the rock-salt structure when the pressure reaches 3.9GPa.[17] Finally, the resulting lattice vibration dispersion, or phonon dispersion curve, as measured using neutron inelastic scattering, is shown [16] on figure 3. The top two bands are the optical phonon bands. Their dispersion curve intersects the photon dispersion, therefore coupling can occur. The lower two bands are the acoustic phonon bands.

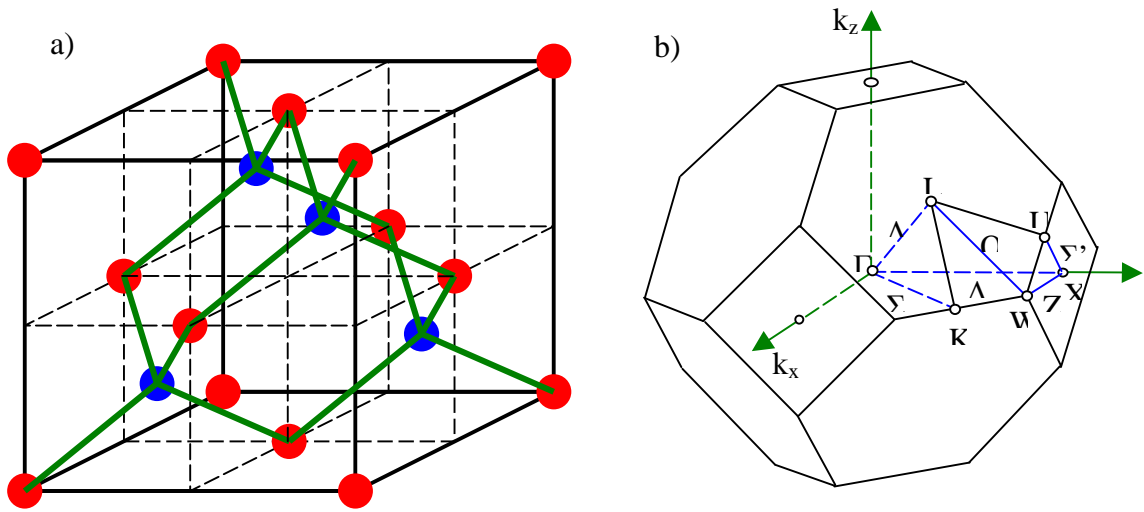


Figure 2: a) Zinblende crystal structure, b) Bravais lattice of the zinblende structure (after [14]).

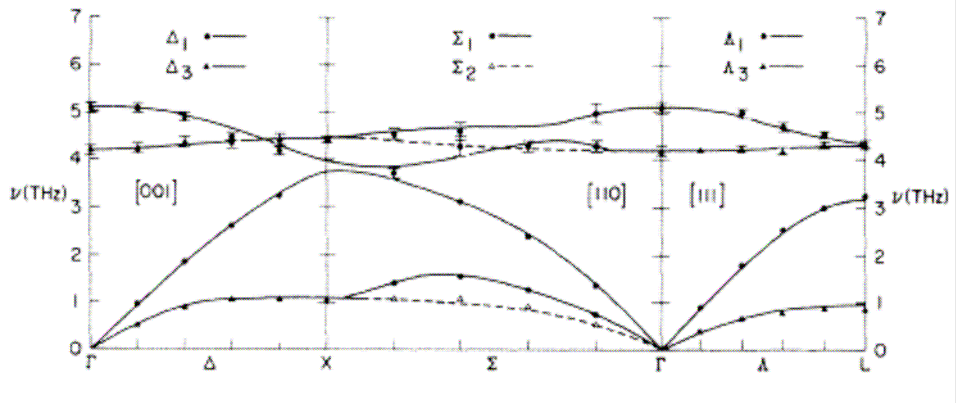


Figure 3: Phonon dispersion curve for CdTe (after [16])

2.1.2. Electronic band structure

2.1.2.1 Theory

The following paragraph summarizes the more detailed study of band structure found in [18], [19] and [20].

In bulk semiconductors, electrons normally located on the outer shell of the individual atoms, i.e. weakly attracted to the nucleus become delocalized and behave as free particles submitted to a periodic potential. Therefore, the eigenfunctions $\psi_\lambda(\mathbf{r})$ of the electron of mass m_0 in the periodic potential $W(\mathbf{r})$ satisfies Schrodinger's equation:

$$\left[-\frac{\hbar^2}{2m_0} \nabla^2 + W(r) \right] \psi_\lambda(r) = E_\lambda \psi_\lambda(r) \quad (2.1)$$

where m_0 is the electron mass, \hbar is the reduced Planck constant, and E_λ are the energy eigenvalues of the Hamiltonian.

Bloch showed that the eigenfunctions $\psi_\lambda(\mathbf{r})$ can be written as the product of a plane-wave envelope $\exp(i\mathbf{k}\cdot\mathbf{r})/V^{1/2}$ and a lattice periodic function $u_\lambda(\mathbf{r})$ called the *Bloch function*. It is obvious from equation (2.1) that knowledge of the potential $W(\mathbf{r})$ is necessary for the calculation of the band structure. However, the problem remains complex. It can be simplified by assuming that the potential is strong enough that the electron is considered localized around an atom, and the overlap between wavefunctions of electrons of different lattices is small. This is called the **tight binding** model. The overall potential $W(\mathbf{r})$ seen by the electron can be written as the sum of the atomic potentials $W_0(\mathbf{r}-\mathbf{r}_l)$ of all the atoms l , where \mathbf{r}_l is the distance between the two atoms.

The wavefunctions $\psi_\lambda(\mathbf{r})$ are written as a linear combination of atomic orbitals (LCAO) or wavefunctions $\phi_\lambda(\mathbf{r})$ which satisfy the simpler, single-atom Schrodinger's equations:

$$\left[-\frac{\hbar^2}{2m_0} \nabla^2 + W_0(r - r_\ell) \right] \phi_\lambda(r - r_\ell) = E_\lambda \phi_\lambda(r - r_\ell) \quad (2.2)$$

Solving these equations and taking into account only direct and nearest-neighbor contributions results in quasi-continuous cosine-shape energy bands $E_\lambda(\mathbf{k})$, whose curvature depends on the atomic functions. Obviously, details of the band structure can only be calculated if the atomic potential W_0 is known. In semiconductors, the highest filled band is called the valence band, while the lowest empty band is the conduction band. They are separated by a small energy gap E_g , of the order of a photon energy.

If the electron were treated as a free particle, i.e. if the potential were null, its energy would be $\hbar^2 k^2 / 2m_0$. Therefore, around the extrema, the **parabolic approximation** can be made for either the electron or hole:

$$E_\lambda(k) = E_\lambda(0) + \frac{\hbar^2 k^2}{2m_{eff,\lambda}}, \quad (2.3)$$

where $m_{eff,\lambda}$ is the effective mass for the λ^{th} band and is defined as:

$$m_{eff,\lambda} = \frac{\hbar^2}{\left. \frac{\partial^2 E_\lambda(k)}{\partial k^2} \right|_{k=0}} \quad (2.4)$$

Equation (2.4) shows that the effective mass increases as the radius of curvature of the band increases.

An energy dispersion curve typical of direct gap semiconductors such as CdTe is shown on figure 4a.[21] The bands are parabolic near the center in first approximation.

The Bloch functions corresponding to conduction states have spherical symmetry (they are s-like) near the center of the Brillouin zone. The valence band states are a linear combination of p-like states. The topmost valence band is divided into a heavy- (larger band curvature) and light-hole bands. The lower valence band arises from spin-orbit splitting of the holes, caused by the high magnetic field seen by valence electrons due to their relativistic velocities and their proximity to the nucleus. The linear absorption coefficient is proportional to the product of the density of states and the transition matrix element, governed by so-called selection rules. The material therefore should be transparent to photons with energies smaller than the bandgap.

While this last statement is generally accepted, transmission measurements at low temperature show features just below the bandgap. This is because up to this point, Coulomb interactions between the electron and hole have been neglected. However, they can bind together and form an exciton.[22] Excitons are hydrogen atom-like particles with a hole and an electron orbiting around their center of mass. If their Bohr diameter is smaller or of the order of a unit cell, they are called Frenkel excitons. In CdTe, the excitons Bohr diameter is larger than the unit cell, and therefore they are called Wannier excitons. Applying the Schrodinger equation to the electron and hole pair with the Coulomb potential $-e^2/|\mathbf{r}_e-\mathbf{r}_h|$, changing the variables of the problem to the center of mass of position \mathbf{R} and total mass M , and the relative coordinate of position \mathbf{r} and reduced mass m_r , and recognizing that \mathbf{R} and \mathbf{r} are independent variables, allows one to separate the problem into two distinct equations. First, the center of mass behaves like a free particle with wave vector \mathbf{K}_c , and its energy is

$$E_R = \frac{\hbar^2 K_c^2}{2M} \quad (2.5)$$

Second, the relative motion of the electron and hole is described by the Wannier equation:

$$\left(-\frac{\hbar^2}{2m_r} \nabla_r^2 - \frac{e^2}{\epsilon_0 r} \right) \phi(r) = E_r \phi(r) \quad (2.6)$$

The solution is similar to the hydrogen atom, and the exciton energy E_x is the sum of the bandgap energy, the center of mass energy and the relative motion energy, that is:

$$E_x = E_G + \frac{\hbar^2 K_c^2}{2M} - \frac{E_B}{n^2} \quad (2.7)$$

where n is an integer strictly positive, and E_B is called the binding energy or the exciton Rydberg energy, and can be written in terms of the exciton Bohr radius a_B :

$$E_B = \frac{e^2}{2a_B \epsilon_0} = \frac{\hbar^2}{2m_r a_B^2} \quad (2.8) \quad a_B = \frac{\epsilon_0 \hbar^2}{m_r e^2} \quad (2.9)$$

The dispersion diagram (figure 4b) of the exciton and equation (2.7) show that photon absorption is possible below the bandgap for energies as low as $E_G - E_B$. Exciton energy levels are parabolic bands whose energies at the center are equal to the Rydberg series. Finally, energies higher than the bandgap correspond to ionization energies, the electron and hole are unbound and the exciton ceases to exist.

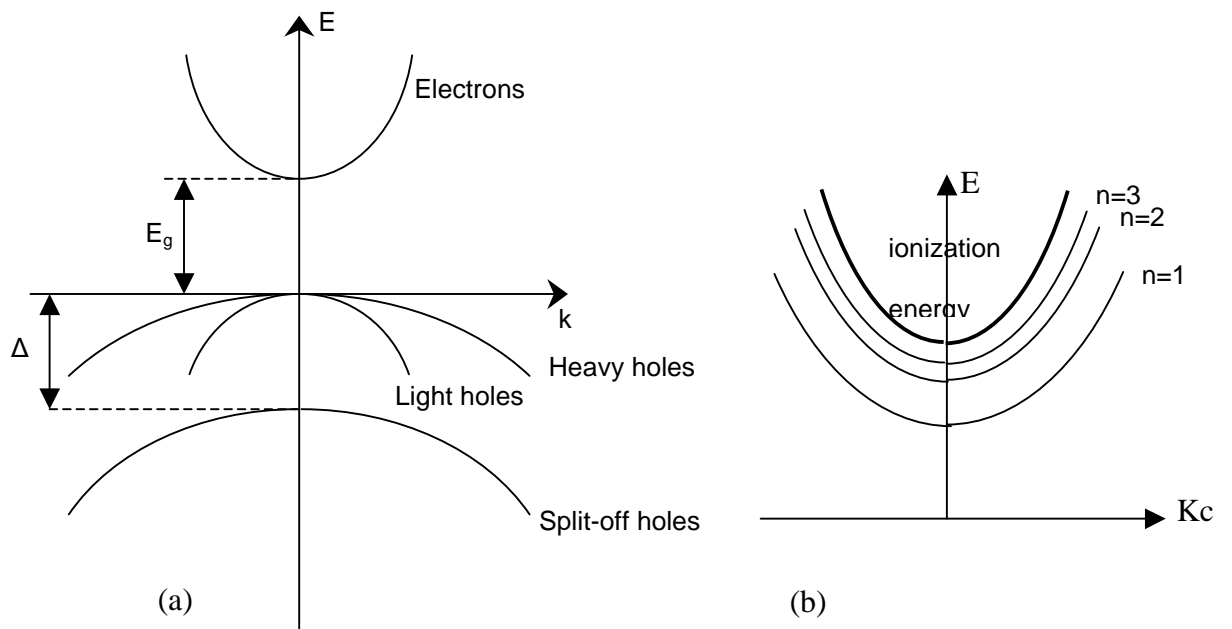


Figure 4: Energy dispersion curves for (a) typical bulk direct-gap semiconductor, [21] (b) exciton in bulk crystal.

2.2.1.2 Band structure of Cadmium Telluride

The electronic band structure of bulk CdTe was calculated by Chelikowski and Cohen [23] using a nonlocal pseudopotential method. A tight-binding model gave similar results.[24] The resulting band diagram is shown on figure 5 and the Bravais lattice for zincblende semiconductors is depicted figure 1b. CdTe is a direct bandgap semiconductor. Chelikowski and Cohen calculated its bandgap to be 1.59 eV.

Magnetoabsorption experiments conducted at 1.64 K gave a bandgap value of 1.6063 eV [25], and reflectivity measurements gave values of 1.55 eV at 90 K and 1.50 eV at 293 K [26]. Spin-orbit coupling causes splitting of the topmost valence band into two bands

separated by 0.89 eV at the center of the Brillouin zone. The electron effective mass in the conduction band is $0.096 m_0$ in the [110] direction [27], $0.094 m_0$ in the [100] direction [28], and $0.095 m_0$ in the [111] direction. The light-hole effective masses are $0.12 m_0$, $0.13 m_0$ and $0.12 m_0$ and the heavy hole effective masses are $0.81 m_0$, $0.72 m_0$ and $0.84 m_0$ in the respective directions. It is also worth noting the flatness of the two topmost valence bands and the lowest conduction band at the L point. This indicates that electron and holes have relatively low velocities and large effective masses at this point. Finally, the exciton binding energy is 10.23 meV and its Bohr diameter is 15 nm [29].

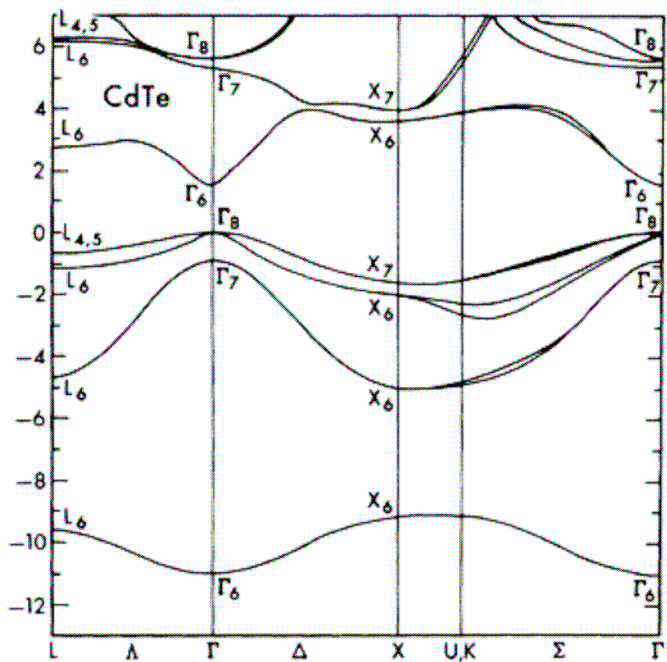


Figure 5: Band structure of bulk Cadmium Telluride [14, 23]

2.2 Effects of confinement on the band structure

As seen in paragraph I.1, loss of dimensionality in semiconductors causes important changes in the density of states distribution and in the bandstructure. Efros [30, 31] gave the theoretical framework for the study of the role of confinement of the electrons and holes for the absorption in spherical quantum dots. He identified three regimes: *weak confinement* in large clusters, *intermediate confinement*, and finally *strong confinement* in small quantum dots. The transition from weak to strong confinement as the quantum dot size is reduced was observed experimentally with absorption spectroscopy.[32, 33]

Quantum dots are considered to be large when their radius a is much larger than the exciton Bohr radius. This is the weak confinement regime. In this case, the binding energy of the exciton (equation 2.8) is much larger than the quantization energy of the electrons and holes (of the order of $\hbar^2 \pi^2 / (2m_{e,h} a_B^2)$). The predominant phenomenon is the confinement of the center of mass motion of the exciton. The center of mass motion is therefore treated as a particle in a box problem with infinitely high potential barriers, in three dimensions and in the spherical symmetry. The exciton energy is:

$$E_x = E_g - E_B - \frac{\hbar^2 \rho_{n,l}^2}{2Ma^2} \quad (2.10)$$

where $\rho_{n,l}$ is the n^{th} root of the l^{th} order spherical Bessel function. The strongest transition is reached for $\rho_{0,0} = \pi$.

The intermediate confinement regime is reached when $a_h < a < a_e$. The spectrum in this case is governed by the motion of the hole about the center of the quantum dot, and submitted to the average potential of the much faster electron.

The work done for this dissertation is situated in the strong confinement regime, where $a \ll a_B$. In a classical interpretation of this case, it can be argued that there is simply not enough room for an exciton to exist in the quantum dot. The electron and holes are confined similarly to the particle in a box problem in spherical symmetry, and their energies are:

$$E_{n,l}^{e,h} = \frac{\hbar^2 \rho_{n,l}^2}{2m_{e,h} a^2} \quad (2.11)$$

where $\rho_{n,l}$ is the n^{th} root of the l^{th} order spherical Bessel function. n is a strictly positive integer, and l is a positive integer. Solving the Schrodinger equation for the wavefunction shows a third quantum number m . The values for l are denoted with the letters s, p, d, ... so that the energy states can be written 1s, 1p etc. Because the electron and hole quantized energies vary as $1/a^2$ and the Coulomb interaction energy varies as $1/a$, the Coulomb interaction can be neglected for small quantum dots, justifying the previous interpretation that the exciton essentially does not exist in strongly confined QDs. The validity of this approximation will be discussed in the next section. In this approximation, selection rules only allow interband transitions with $\Delta l=0$. The lines energies E^{abs} are therefore:

$$E_{ne,nh,l}^{\text{abs}} = E_g + \frac{\hbar^2 \rho_{ne,l}^2}{2m_e a^2} + \frac{\hbar^2 \rho_{nh,l}^2}{2m_h a^2} \quad (2.12)$$

This model is known as the parabolic approximation, because the carriers in this model are not subjected to any potential other than the confinement potential, which would result in the bulk in parabolic bands. To fully describe the bandstructure in CdTe quantum dots though, one needs to account for the real structure of the bulk, that is, the non-parabolicity of the bands, the complicated bandstructure of the holes (light and heavy holes, split-off band) and mixing between the valence and conduction states induced by confinement. These concerns were addressed in the effective-mass approximation (EMA) which is discussed below. An alternate method [34, 35] was developed within the tight binding model, in part to address the limitation of the infinite confinement potential, but did not prove to be as popular as the EMA approach.

A four band model (accounting for spin degeneracy) of the valence band with distinct heavy-hole and light-hole bands, but neglecting the spin-orbit split-off band by setting the split-off energy either to zero or to infinity, was first studied by Xia [36] using the envelope function approximation with the Baldereschi and Lipari [37, 38] Hamiltonian. Koch [39] found that band mixing was occurring between the light-hole and heavy-hole states, meaning that these states are not eigenstates in the quantum dot. Calculations show that strong variations occur in the bandstructure as the band coupling varies from one valence band to two bands to the limit of an infinitely heavy-hole band. A third important result is that previously forbidden selection rules become allowed. This model also agrees with the experimental observation that, contrary to the 1-parabolic band model, AlGaAs QD heterostructures have optically isotropic properties.[40] In the

simpler approximation of degenerate heavy- and light-hole bands, ellipticity of the quantum dots induces splitting of the bands.[41]

Ekimov [42] first included finite split-off energy (the so-called 6-band model) in the band calculation of QDs in the intermediate confinement regime, and Richard and Lefebvre [43, 44] studied its role in strongly confined QDs. The mixed lh-hh states are now replaced by mixed lh-hh-SO states. This mixing occurs even with large split-off energies, such as in CdTe. The higher energy valence states are similar to the states obtained from the previous model. However, higher-order states strongly depart from earlier model in that their confinement energies are not directly proportional to $1/a^2$ anymore. Photoluminescence excitation (PLE) and persistent spectral hole burning (PSHB) data came also in support of this model,[45] especially at higher energies, where the 6-band model departs most from the 4-band model. PSHB compares the absorption spectrum of the sample before and after excitation of the lowest transition in the sample with a strong laser pulse. Peaks at higher energies are interpreted as energy levels. PLE consists in measuring the intensity of the photoluminescence emitted at fixed wavelength as a function of the lower excitation wavelength.[46] This technique provides somewhat higher resolution in samples with broad size distributions because it has better size selection as the excitation wavelength decreases. In addition, it was found by others[47] that asphericity of the QD causes an increase in the split-off energy.

Finally, Efros and Rosen [48] showed that the valence bands also couple with the conduction bands even in the case of wider gap semiconductor such as CdS (whose bandgap is 60% larger than CdTe). Therefore, the 8-band model best describes its

bandstructure. They decided to denote the electron and hole states nQ_j , where n is the ordinal number with a given symmetry, Q is the lowest value of L , the envelope angular momentum, in the wavefunctions and is denoted S, P, D..., and j is the total angular momentum. Selection rules state that Q must be conserved in hole to electron transitions. The calculated bandstructure of CdTe according to this model is shown on figure 6. The first three electron levels are in the following order: $1S(e)$, $1P_{1/2}(e)$, and $1P_{3/2}(e)$. The $1P$ states are almost degenerate. The order of the hole level varies with their size, but at 20 \AA it is the following: $1S_{3/2}(h)$, $1P_{3/2}(h)$, $2S_{3/2}(h)$, $1P_{1/2}(h)$, $2P_{3/2}(h)$, $1S_{1/2}(h)$ etc...

State notation conventions do vary in the literature as a function of the model and the authors; this dissertation will use the above convention.

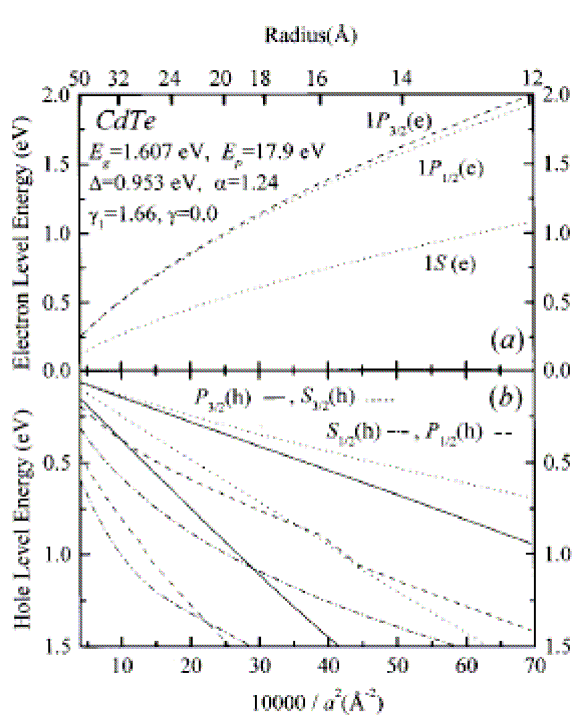


Figure 6: Bandstructure of CdTe quantum dots calculated in the 8 parabolic band model[48]

2.3 Excitonic effects in the strong confinement regime

The effective mass approximation predicts well absorption spectra of quantum dots. However, the observation of red-shifted photoluminescence with respect to the band edge absorption is subject to controversy.[49] Some explain it by the presence of excitons, while others see the effect of surface states. Excitonic effects will be explored in this paragraph, while surface effects will be discussed in the following section.

It was stated earlier that because the confinement energy varies as $1/a^2$ and the Coulomb interaction varies as $1/a$, the Coulomb interaction could be neglected in the strong confinement regime and the electron and hole could be treated as uncoupled.[30] However, Brus showed [50] that the Coulomb interaction does shift the absorption lines to the red by approximately $1.8 e^2/(\epsilon a)$, where ϵ is the permittivity of the material. More importantly, surface polarization effects created by an incident electric field decrease the symmetry of the model introduced by Efros, and as a result, the Coulomb interaction in QDs is different than in bulk semiconductors.

Applying a numerical matrix diagonalization scheme to the degenerate valence band effective mass approximation, Hu [51] showed that, in addition to these small energy shifts, the Coulomb interaction modifies the selection rules. He argued that, in the sense that Coulomb interactions affect electron-hole pairs, the term exciton can be used “loosely”[51] for one-pair states, and biexciton for two-pair states in the strong confinement regime. But it is important to understand that, besides Coulomb-induced shifts and different selection rules, there are no additional excitonic peaks in the absorption spectrum of strongly confined QDs as could be observed in weakly confined

QDs or in the bulk. Calculations of the radial distribution functions of the electron and hole clearly show that the Coulomb interaction pushes the hole to the center, and the electron to the side. It is this asymmetry that creates a change in selection rules. On the other hand, the strictly positive biexciton binding energy increases with the confinement, proving that Coulomb effects do matter in the strong confinement regime. The biexciton binding energy δE_2 is defined as:

$$\delta E_2 = 2 E_1 - E_2 \quad (2.13)$$

where E_1 and E_2 are the exciton and biexciton ground state energy. Without taking the interaction into account, the binding energy vanishes with confinement. This issue had been previously explored by Efros[52] and Takagahara[53].

These two modifications brought by Coulomb interaction imply nonlinear effects for the quantum dots. The best proof for the role of biexcitons [54-57] resides in the induced absorption of the high energy side of the lowest transition in differential transmission spectrum (DTS) experiments previously observed by Peyghambarian.[58, 59] DTS compares the transmission of a white, ultrafast probe pulse before and after a stronger, monochromatic ultrafast pump pulse. The coupling between non-degenerate heavy- and light-hole bands (in the 4-band model) induces significantly different radial distribution functions for the holes[39], and causes the ground-state exciton energy to decrease.[60] Coupling, as confinement, also increases the binding energy of the biexciton. The biexciton binding energy in $\text{CdS}_x\text{Se}_{1-x}$ was measured by DTS [61] and fit to Hu's model, and both contributions from Coulomb interaction and light- and heavy-hole band couplings were observed in two-photon absorption experiments in CdS.[62]

The fine structure of the band-edge exciton in CdSe and CdTe quantum dots, defined as the first electron-hole pair, was also investigated.[49, 63] In the effective mass approximation, it is eightfold degenerate. This degeneracy is lifted by three phenomena. First, perturbation theory shows that an elliptical shape of the quantum dot splits the exciton state in two fourfold degenerate states.[41] The separation increases with confinement, and depends on the ratio of the hole effective masses. The average energy of the exciton does not shift though. Second, in the particular case of CdSe, the wurzite crystal structure causes splitting of the exciton as well.[64] Third, because confinement increases the overlap between electron and hole wavefunctions, it tends to increase as well their exchange interaction.[65] This interaction creates splitting of the exciton as well.[66, 67] When considered together, these three effects result in the eightfold degeneracy being split between five states.[49] Those states are denoted $F^{U,L}$, where F is the projection of the total angular momentum, and U and L denote upper and lower. The states are ± 2 , $\pm 1^{U,L}$, and $0^{U,L}$. Because photons cannot have a momentum of ± 2 , these states are optically passive. Calculations of the optical excitation or recombination probabilities reveal that in CdTe the upper 0 and ± 1 states are optically active, the lower 0 state is optically passive, and the lower ± 1 states are passive in spherical dots and active in elliptical dots. The size dependence of the energy levels of the eight states is shown on figure 7. It is worth noting that, in CdTe spherical crystals, the exciton state is split between only a higher energy, threefold degenerate, optically active state and a lower energy, fivefold degenerate optically passive state. The optically active states are deemed “bright excitons” while the optically passive states are deemed “dark excitons”.

Experimental evidence of the bright excitons was found in photoluminescence excitation (PLE) and fluorescence line narrowing (FLN) measurements.[63] These techniques help reduce broadening due to sample inhomogeneities. Photoluminescence experiments, once corrected for a shift due to crystal size distribution,[49] reveal coupling between the LO-phonon and the dark ± 2 excitons. The long decay of the dark exciton was observed under magnetic field.[66]

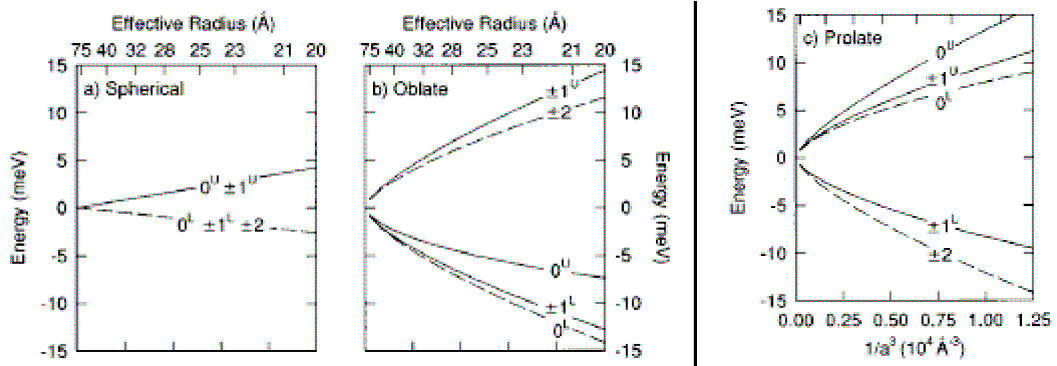


Figure 7: Size dependence of the exciton sublevels [49]

2.4 Role of traps and surface states

It is well known that in bulk semiconductor crystals, impurities and defects, even at low concentration, can dramatically alter the properties of the crystal by introducing donor or acceptor states in the bandgap. Indeed, the broad luminescence peak at long wavelengths often observed in QD-doped glass is attributed to deep trap levels.[68] It has been shown [69] that bulk wurtzite CdSe surfaces have surface valence bands created by lone Se pairs just below the top of the valence band. Moreover, surface Cd atoms also create states, but further in the conduction band. Bawendi [70] argued that these hole

surface states mix with the lowest hole confined state as confinement occurs. The hole would be localized on the surface. In fact, he argued [46] that the observed 100 ns photoluminescence emission decay of chemically prepared [71] CdSe quantum dots was too long compared to the estimated ns decay of a purely radiative recombination of a $1s_e-1s_h$ transition. He attributed instead PL emission to the localization of carriers on surface states. This hypothesis had been evoked earlier.[72, 73] The mixed surface-confinement hole states create a broad, deep-trap band, explaining the observation of a second, broader, longer wavelength peak in photoluminescence experiments.

However, Bawendi later dismissed this surface model. First, he tested it with transient differential absorption (TDA) experiments [74] on high quality colloidal CdSe samples. It was found that the strength of the narrow bleach peak and the long radiative lifetime of the photoluminescence peak are in contradiction in the surface state model. However, if the fine structure of the exciton level is taken into account, it can be argued that the slow decay time is explained simply by inefficient coupling of the ± 2 dark excitons and phonons. Second, in a different set of experiments, he compared the luminescence of high quality samples that had received various surface treatments.[75] The independence of the data on the surface treatment and the good fit with the fine structure of the exciton led the authors to dismiss the surface model.

More recent data tends to suggest that, even though intrinsic surface states do not play a role as stated above, induced surface traps do. The spectral dependence of PL decay times in CdSe QDs as well as low PL intensities indicate the dominant role of surface traps.[76] The surface was also found to play a role on the quantum efficiency of

the room temperature PL emission of CdTe QDs.[77] Indeed, fast grown colloidal CdTe with excess surface Te have lower PL quantum yield than quantum dots created in dynamic equilibrium.[78] Traps can also be formed in semiconductor-doped glasses if the stoichiometry between Cd and Te is not respected.[79] Evidence of excess Te can be found in the transmission spectrum, while excess Cd is seen in the PL spectrum. Kang [80] noted the importance of the surrounding medium for a quantum dot since glass modifiers in the matrix provide defect sites. Klimov was able to separate the contribution from holes and electrons to the decay rate in glass-doped [81] and colloidal [82, 83] CdSe QDs and suggested that holes relax through intrinsic trap sites while electron relaxation is driven by surface defects, though not by crystal size. Finally, recent up-conversion, or anti-Stokes, photoluminescence of CdTe quantum dots was attributed to surface states [84-86], and more generally localized trap states,[87] but the eventual role of the fine structure of the exciton was not discussed.

2.5 Phonon effects

The role of phonons in the continuous-wave (cw) and ultrafast optical properties of quantum dots has been investigated. Electron-phonon effects in bulk semiconductors are well known,[88, 89] and in II-VI semiconductors in particular, intraband carrier cooling is accomplished mostly through electron – longitudinal optical (LO) phonon longitudinal interaction, via Froehlich coupling.[90, 91] This relaxation mechanism is made possible because of the quasicontinuous nature of the electron and hole dispersion

curve and because the LO phonon curve is relatively flat. In quantum dots, the bands are discrete, and their energy separation increases with confinement. Therefore, multiple phonons would be required for energy relaxation, slowing down the process considerably. This should create a “phonon bottleneck”.[92, 93] However, many studies report no slowdown consistent with this bottleneck for electron relaxation,[82] though it has been observed for holes in CdSe.[94] The following paragraph will address this discrepancy.

2.6 Auger effects

The energy released by the relaxation of an electron to a lower available state in an atom, or electron-hole pair recombination in a quantum dot, can result in the emission of a photon or a phonon, or into the autoionization of the atom or QD, as shown on figure 8. This latter mechanism is called Auger process.[95] Autoionization of the quantum dot results in the ejection of an electron or hole into a trap state on the surface of the quantum dot [96] or in the glass matrix. The carrier can also be promoted to one of the higher confined levels with the emission of a phonon or absorption of a phonon to satisfy energy conservation.[97] The Auger process is responsible for the slow decay [98] in the cw PL intensity of QD-doped glasses: two-photon excitation of the QD [99] leads to its ionization through Auger recombination of one electron-hole pair. The ionized QD cannot luminesce because the extra electron or hole absorbs the energy released by subsequent electron-hole recombinations. Luminescence can only occur after thermal

diffusion of the ejected carrier back to the QD.[95] The initial two-photon absorption of this process makes it intensity dependent.

The Auger process considerably speeds up the relaxation of the non ejected carriers in QDs and has been found to break the aforementioned phonon bottleneck,[81, 100] resulting in actual recombination rates on the order of picoseconds. Numerical evaluation [101] and experimental measurements [99] of the Auger recombination rate in CdS QDs show that it rapidly increases when the crystal radius decreases, and varies as $1/a^v$, with v varying from 3,[97] to 5 to 7.[95, 101] This is due to different reasons. First, Auger transitions are governed by electron-electron Coulomb interactions, therefore, they should be more important as confinement increases. Second, momentum conservation rules in the bulk are replaced by laxer angular momentum conservation rules at the QD boundaries. Finally, the surface to volume ratio is important because the carrier has maximum kinetic energy on the surface, making it more likely to be ejected.

If the quantum dot samples are treated like bulk samples, i.e. if a large number of electron-hole pairs are considered, the Auger decay rate is a cubic process since it involves three particles, and it can simply be written as $-CN^2$.[102] This model gives satisfactory fits to photoluminescence measurements,[103] pump-probe measurements,[104] and more sensitive transient degenerate four-wave mixing and nonlinear absorption experiments.[105] Even if quantum dots with no more than four electron-hole pairs are considered,[97] and the rates of decay from 2-pair states, 3-pair states, and 4 pair states are carefully separated, the cubic dependence is confirmed.

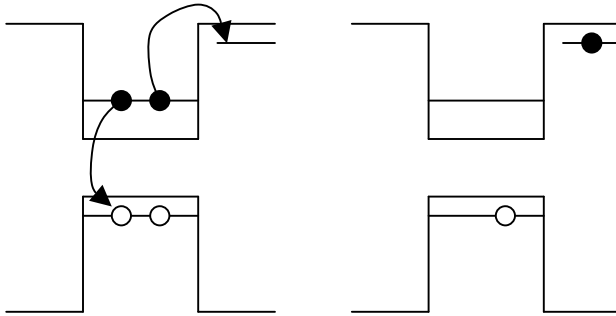


Figure 8: Auger autoionization mechanism: the energy released by the recombination of the first electron-hole pair is used to eject the electron in a continuum of states on the surface or in the surrounding glass matrix

CHAPTER 3

EXPERIMENTAL TECHNIQUES

3.1 Sample fabrication

Films were deposited by a previous student [106, 107] and heat treatment was performed for this study. The following paragraph will provide an overview of the fabrication process. More details can be found in [106].

The samples consisted of CdTe crystallites dispersed in a glass thin film on a glass substrate. Silica slides were used as the substrate. The film was deposited using a dual-source R-F magnetron sputtering technique, which worked as follows. The deposition chamber is pumped by a turbomolecular pump to a 10^{-6} Torr vacuum. Two substrates are alternatively exposed to two targets. The relative exposure time, or duty cycle, will eventually determine the final film composition, and the two compositions will be complementary. Each substrate is placed on an anode, and is facing a target, which is placed on a cathode. The chamber is filled with Argon gas at a pressure of 3 mTorr, with a flow of 20 sccm. A voltage is applied between anode and cathode. Because both substrate and target are insulating, the voltage cannot be DC, but is rather at 13.57 MHz, in the radio frequency part of the electromagnetic spectrum. The voltage creates a self-sustaining plasma at the cathode in the following manner: secondary electrons are ejected from the cathode, collide with and ionize argon atoms, which in turn bombard the

cathode and create secondary electrons. Bombardment of the cathode by argon ions is responsible for the sputtering process, i.e. ejection of atoms from the target towards the substrate. The plasma, and thus the deposition rate, is controlled using two main variables: voltage and argon pressure. A high voltage means high electron kinetic energy resulting in a higher number of collisions per electron. Gas pressure must be high enough so that the electron mean free path is kept small and the number of collisions is maximized. However, if the gas pressure is too high, the energy of the bombarding ions will decrease, and, separately, the number of impurities will increase. But the gas pressure may be kept low if the electron trajectory can be maximized and confined. This is accomplished with a magnetic field in the cathode area.

The targets used were 99.999% CdTe and Pyrex 7740. The voltage was adjusted for the deposition rate to be $1 \text{ \AA}/\text{s}$. The duty cycle was adjusted for a 5% volume CdTe composition. 88 cycles were used, and the final film thickness was approximately $2.2 \text{ }\mu\text{m}$. Rapid thermal annealing (RTA) was performed in the chamber using a halogen lamp for 30 s at 515 C. Finally, the samples were heat treated in a tube furnace at 600C and 650C for up to 18 hours.

	Heat treatment
Sample 1	RTA
Sample 2	RTA + 2 hours at 600 C
Sample 3	RTA+ 14 hours at 600 C
Sample 4	RTA + 18 hours at 650 C

Table 1: Heat treatment of the various samples.

3.2 Sample characterization

3.2.1 Transmission spectroscopy

3.2.1.1 Instrumentation

The transmission spectrum of the samples was recorded using a double-beam Perkin-Elmer Lambda 950 spectrometer from the ultraviolet to near-infrared region. The region of interest actually lies in the red. The UV end was chosen so results could be easily compared to previously published data on blue shift due to confinement at the L-point [108], and the spectrum was measured in the NIR because the low absorption in this region simplifies the task of fitting interference fringes. The reference sample was a bare substrate, identical to the one on top of which the films were deposited. The absorption coefficient was calculated using the model described in the following paragraph.

3.2.1.2 Multiple beam interference model

The multiple beam interference from a parallel film known as Fabry-Perot oscillations is well known and its solution in terms of the Airy function is derived in textbooks such as [109]. However, the geometry of the problem is generally a thin film with air on both sides. This symmetry is lost if the thin film is deposited on a thick substrate such as shown on figure 9. An expression for the transmittance of the entire assembly is derived in the following paragraph.

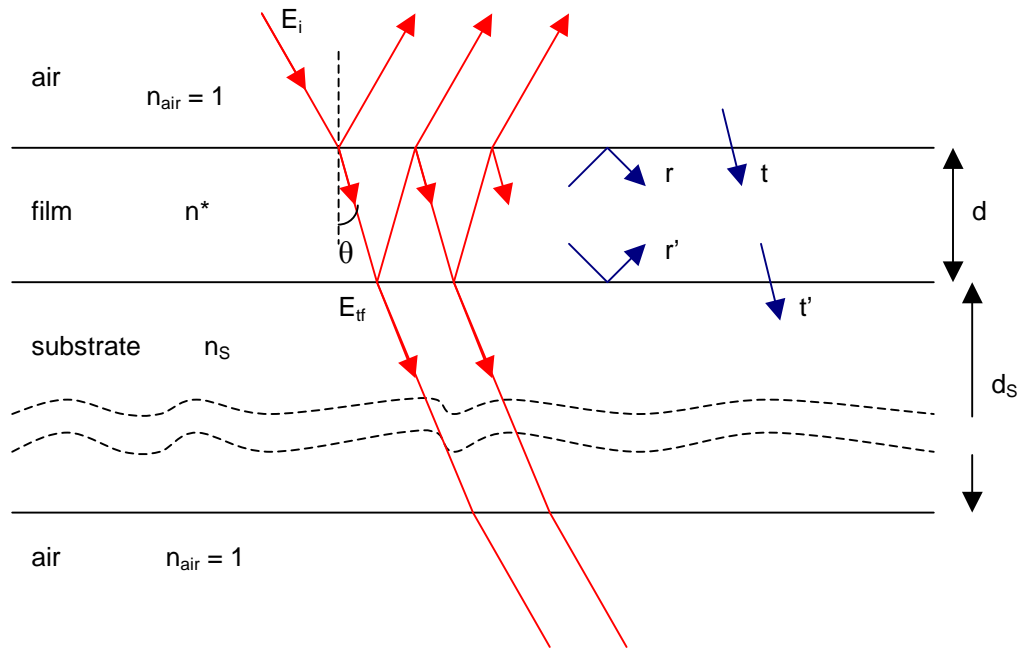


Figure 9: Interference on a thin film deposited on a substrate

The beam propagates in the film at an angle θ with the normal. The phase change δ undergone by the electric field after each roundtrip in the film is:

$$\delta = 2\pi / \lambda_0 2 n d \cos \theta \quad (3.1)$$

In addition, the field is attenuated according to Beer's law after each roundtrip by a factor of $e^{-\alpha d \cos \theta}$. The transmitted field E_{tf} just after the film can be calculated by the geometric sum as:

$$\frac{E_{tf}}{E_i} = tt' e^{-\frac{\alpha d}{2}} e^{i\frac{\delta}{2}} \sum_{N=0}^{\infty} (rr' e^{-\alpha d} e^{i\delta})^N = \frac{tt' e^{-\frac{\alpha d}{2}} e^{i\frac{\delta}{2}}}{1 - rr' e^{-\alpha d} e^{i\delta}} \quad (3.2)$$

In the case of normal incidence ($\theta=0$), polarization does not matter, and the transmission and reflection coefficients can be taken as the parallel coefficients. Furthermore, absorption in the film can be accounted for by using the complex index of refraction for

the film: $n^* = n + i\kappa$, where $\kappa = \alpha \lambda_0 / (4\pi)$. The phase of the transmission coefficients can be discarded since equation (3.2) will be multiplied by its complex conjugate. The coefficients are as follows:

$$t = \frac{2}{\sqrt{(n+1)^2 + \kappa^2}} \quad (3.3)$$

$$t' = 2\sqrt{\frac{n^2 + \kappa^2}{(n+n_s)^2 + \kappa^2}} \quad (3.4)$$

$$r = \frac{1-n-i\kappa}{1+n+i\kappa} = \sqrt{R}e^{i\gamma} \quad (3.5)$$

$$r' = \frac{n_s - n - i\kappa}{n_s + n + i\kappa} = \sqrt{R'}e^{i\gamma'} \quad (3.6)$$

If no film is on the substrate, the transmission coefficient at the first air/substrate interface is:

$$\frac{E_{tS}}{E_i} = t_s = \frac{2}{n_s + 1} \quad (3.7)$$

Multiplying equation (3.2) by its complex conjugate, recognizing that $\cos\delta = 1 - 2\sin^2\delta$, and dividing by equation (3.7) squared, we obtain an expression similar to the Airy function:

$$\frac{T}{T_s} = \frac{T_0}{1 + F \sin^2 \frac{\delta + \gamma + \gamma'}{2}} \quad (3.8)$$

Where T is the total transmittance of the film and the substrate, T_s is the transmittance of the substrate alone, and T_0 and F are given by:

$$T_0 = \frac{e^{-\alpha d}}{t_s^2} \left(\frac{tt'}{1 - \sqrt{RR'}e^{-\alpha d}} \right)^2 \quad (3.9)$$

$$F = 4 \frac{\sqrt{RR'}e^{-\alpha d}}{(1 - \sqrt{RR'}e^{-\alpha d})^2} \quad (3.10)$$

In a final important remark, it can be shown that, if $n = n_s (1+x)$ where $x \ll 1$, and in the absence of absorption, the normal transmittance can be written as:

$$\frac{T}{T_s} = 1 + x \frac{n_s - 1}{n_s + 1} \cos \left(\frac{2\pi}{\lambda_0} 2n_s (1+x)d \right) \quad (3.11)$$

In other words, if the substrate's index is known but the parameter x and the film thickness are unknown, the fringe amplitude is proportional to x , and the fringe spatial frequency is proportional to $(1+x)d$, if the dispersion of the film follows the dispersion of the substrate.

A solution for $\text{GeO}_2\text{-SiO}_2$ films deposited on a SiO_2 substrate is given in reference [110] that takes into account the index dispersion of the substrate and the film. In the presence of index dispersion, the fringe spacing varies and the resulting absorption curve becomes difficult to analyze without a good guess of the index of dispersion of the film. If the substrate is silica glass, its index dispersion is known. [111]

3.2.2 Photoluminescence measurements

Photoluminescence measurements were performed at room temperature using an argon ion operating at 514 and 488 nm laser and a Raman spectrometer. The light source was a Spectra-Physics 2020 laser. It is a multi-line continuous-wave argon ion laser operating at a maximum power of 1W. This laser was chosen because of its relatively high photon energy. The gain medium is low-pressure Argon gas tubes.[112] A plasma is created by collision of the argon atoms with electrons generated by a heated cathode. A magnetic field is needed to keep the electrons within the plasma tube. The high temperature of the plasma requires important water cooling. Electron collisions excite the atoms to the actual Ar^+ ground state. Further collisions pump the ions to excited states. The ion and the excited state form the ground and the highest level of a four-level laser. Various levels between the two are available, resulting in a variety of lasing wavelengths

between 400 nm and 600 nm. The cavity is a stable 2-mirror cavity, to which a prism was added for single-wavelength operation. The laser was used at 514 nm and 488 nm.

The spectrometer was a Jobin-Yvon Horiba LabRam HR coupled to an Olympus IX microscope. The laser beam is first filtered for plasma lines by a dielectric filter. A computer-controlled neutral density filter wheel lets the user adjust the beam intensity. The beam is then reflected off a holographic notch filter centered on the laser wavelength and adjusted at the optimum angle towards the microscope. The microscope objective is used to focus the excitation laser line and for collection of the scattered and luminesced light. A CCD camera was used for sample and beam alignment. That light follows the same path as the laser beam toward the notch filter where it is transmitted, and where the Rayleigh line is filtered by reflection. The actual spectrometer is a Czerny-Turner monochromator. The incident light was focused on the computer-controlled entrance slit. A first cylindrical mirror collimated the scattered light toward a grating. The dispersed spectrum was then imaged by a second cylindrical mirror onto a thermo-electrically cooled CCD.

Laser alignment was checked daily. A sample of silicon wafer was placed under the microscope. A red diode located below the CCD turned on, and the grating was rotated to the diode wavelength, so it could be imaged on the monitor. Two external routing mirrors were adjusted so the laser would focus on the same spot as the diode, and so that the defocused beam's airy pattern was uniform in intensity. Spectrometer calibration was performed daily using the grating's zeroth order and a well known line (here, the silicon line at 520 cm^{-1}).

3.3 Ultrafast measurements

3.3.1 Laser system description

A schematic of the laser system is provided in figure 1. It had three main stages. First, 80-fs long ultrafast pulses but low in energy (10 nJ pulse energy) were generated using a Ti:sapphire oscillator. The pulses then had to be amplified in a second stage in order to seed an optical parametric amplifier needed to generate the tunable pulses.

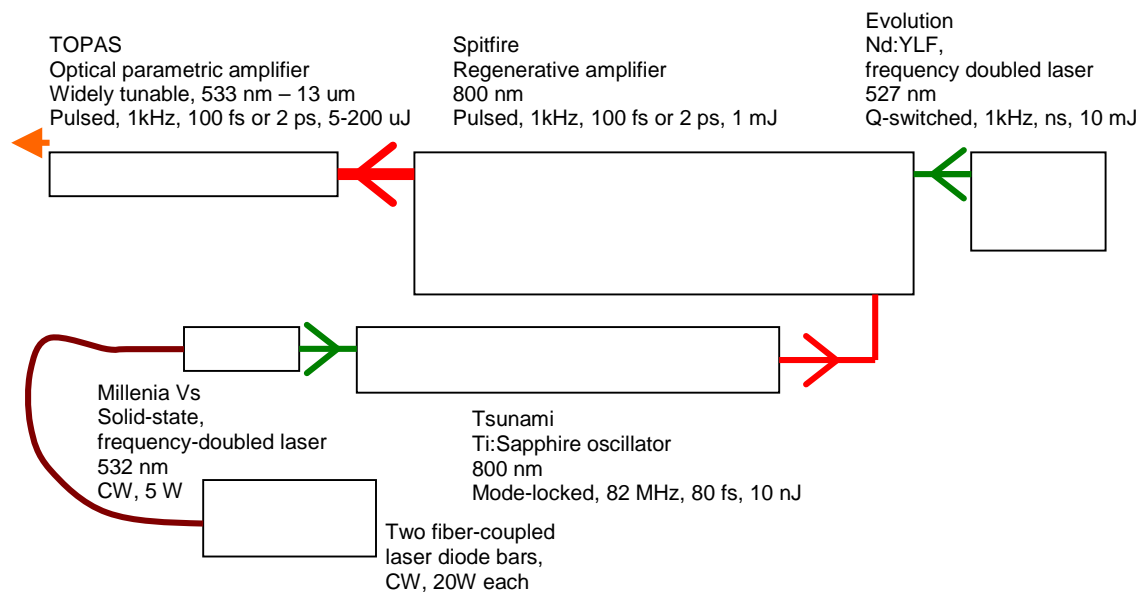


Figure 10: Laser system

3.3.1.a. Ultrafast pulse generation

The laser used to pump the oscillator was a Spectra-Physics Millenia Vs.[113] It is a solid-state continuous-wave laser emitting at a wavelength of 532 nm and at a specified power of 5 W. The gain medium is a neodymium-doped yttrium vanadate crystal (Nd:YVO_4). The active medium is the Nd^{3+} ions, and it is used in a four-level

transition scheme. This medium is itself optically pumped using two 20 W diode bars lasing at a wavelength in the neighborhood of 810 nm, matching one of the absorption bands of the Nd^{3+} ions. The advantage of laser diode pumping over the older flash lamp technique resides in better pumping efficiency due to better spectral overlap, resulting in much lower heat generation, as well as longer lifetime of diodes over flash lamps. The laser diodes are coupled to a fiber optic bundle for delivery of the laser beams to the vanadate crystal, where they are focused so as to match the Millennia's mode for efficient pumping. The vanadate crystal's laser transition occurs from the ${}^4\text{F}_{3/2}$ to the ${}^4\text{I}_{1/2}$ transition, resulting in a photon emission at 1064 nm. [add band diagram ? Weber p8] Green light is obtained by frequency-doubling of the 1064 nm photons. An intracavity temperature-tuned lithium triborate crystal is used for that purpose. Chaotic noise problems usually associated with that technique are addressed in part by increasing the cavity's length, resulting in a much higher number of axial modes, thus averaging out the noise in individual modes. Finally, the green light is coupled out using a dichroic mirror.

The actual ultrafast pulses were generated using a Spectra-Physics Tsunami laser. It is a mode-locked, Ti:Sapphire laser operating at a wavelength of 800 nm, a repetition rate of 82 MHz and a typical pulse energy of about 10 nJ. The gain medium of the laser is a Ti^{3+} -doped sapphire (aluminum oxide) crystal, and the active medium is the titanium ions. It is the medium of choice for ultrafast applications because it has broadband, homogeneously broadened gain.[112] This need is dictated by Heisenberg's uncertainty principle, or it can be understood by a simple Fourier transform between time and frequency spaces. Sapphire is also known for its very good mechanical (high hardness

and rigidity) and thermal (high thermal conductivity) properties. The ground state 2T_2 as well as the first excited state 2E of the T^{3+} ions consists of a series of overlapping vibrational levels, effectively consisting of homogeneously broadened bands. Absorption of the 532 nm pump photons occurs between the lowest of the 2T_2 states and some higher 2E states. These states then rapidly relax to the lowest states within this band. Photon emission occurs during the decay from this state to a variety of the ground states, which finally relax to the lowest ground state. Therefore, the crystal behaves like a 4-level system with a broad gain curve. Wide gain is necessary for obtaining ultrashort pulses.

The cavity was designed so as to allow a high number of harmonics to travel in phase so that they can overlap and form ultrashort pulses. The first step is to obtain a maximum of longitudinal modes. This is possible by maximizing the cavity length, which, under usual constraints of space in a laboratory environment, resulted in a cavity folded in Z. The reason behind this requirement is that the longer cavity (i.e. a high number of longitudinal modes), the lower the repetition rate of the laser, resulting in higher energy per pulse.

A second important component of the cavity is a group velocity dispersion (GVD) compensation mechanism. Because 100 fs pulses are up to 15 nm wide in wavelength, dispersion of optical cavity elements causes bluer harmonics to see longer optical paths than redder harmonics, effectively stretching the pulse at each pass. This is called group velocity dispersion. Hence a device is required to compensate for this path difference. Spectra-Physics uses a set of four silica prisms arranged as shown on figure xxx. Prisms have the advantage of being very efficient dispersive optical components contrary to

gratings. Because the index for the red harmonics is lower than that for the blue harmonics, they undergo less deviation when they travel through the first prism. The second prism sets the harmonics parallel to each other again but separated in space, while the last prism pair is arranged symmetrically to the first one, and recombines the harmonics in space. However, the blue harmonics have traveled a shorter optical distance, allowing them to catch up with the red ones. Translating the middle prisms in and out of the beam lets the user tune the amount of GVD compensation to obtain the shortest pulse, while a slit located in the middle of the two lets the user select which harmonics to use, therefore tune the pulse central wavelength.

The third crucial cavity element is an active mode-locking device in order to keep the harmonics in phase. This is achieved with an acousto-optic modulator (AOM), consisting of a quartz crystal attached to a piezoelectric transducer. The transducer can be used to create a standing acoustic wave across the crystal, creating a phase grating. Since the grating diffracts some of the beam power, it creates sufficient loss to prevent any lasing in the cavity. Hence the AOM can be seen as a controllable optical switch. Lasing is possible only when the AOM is off. The switch is not used to build up gain in the cavity, but rather to force all the harmonics to be in phase. The AOM turns on and off at the cavity's natural repetition rate, and only opens to let the pulse travel back and forth within the cavity. To ensure proper mode locking, the AOM's frequency is driven by a photodiode inside the cavity. This technique is called regenerative mode locking.

The output of the Ti:Sapphire oscillator was reflected off a beamsplitter to seed a regenerative amplifier. The transmitted portion of the beam was fed into a spectrum

analyzer. This ensured that the pulses had sufficient bandwidth and - most important - that there was no continuous-wave (CW) breakthrough. Such breakthroughs may damage the amplifier and are very hard if impossible to detect using autocorrelation techniques.

3.3.1.2. Pulse amplification

The laser used to pump the regenerative amplifier is a Spectra-Physics Evolution X. It is a solid-state, Q-switched laser operating at a wavelength of 527 nm, a repetition rate of 1 kHz, and an average power of up to 10 W. Pulse duration is on the order of the nanosecond. The gain medium is a neodymium-doped yttrium lithium fluoride crystal (Nd:LiYF₄ or, more commonly, Nd:YLF), and the active gain medium is the Nd³⁺ ions. Just like in YVO₄ crystals, the lasing transition is between the ⁴F_{3/2} and ⁴I_{1/2} levels, but they are 1054 nm apart here. Again, the gain medium is pumped by laser diodes. However, they are placed in the cavity, on the sides of the rod. The laser light is frequency doubled by an intracavity lithium triborate crystal, which, when used with a dichroic filter transmitting the green, acts as an output coupler. Pulses are generated with the help of an AOM acting as a Q-switch. First, the AOM is turned on, creating high losses in the cavity. The laser diodes are kept on as well, progressively pumping the laser rod, and building up gain. Because the upper energy state has a relatively long lifetime (470 us), energy can be stored on that level. When the AOM is turned off, the gain far outweighs the losses in the cavity, generating a giant pulse.

The regenerative amplifier is a Spectra-Physics Spitfire. It outputs 100 fs long pulses at a wavelength of 800 nm, with a maximum energy of 1 mJ at a repetition rate up to 1 kHz. It is seeded by the Tsunami and pumped by the Evolution. The main issue with regenerative amplifiers is that the amplified pulse peak power is so high that it self-focuses in the Ti:Sapphire rod resulting in damage if the amplifier was directly seeded by the oscillator. The solution, called chirped pulse amplification, consists first in stretching the pulse's duration before amplification of its spectral components, and then in compressing the amplified pulse to its original duration. The seed enters the stretcher after going through a Faraday isolator. The main component of the stretcher is a grating which is passed four times by the beam. The grating is set up so that after the four passes, the bluer harmonics have traveled a longer path than the redder harmonics, and all the harmonics are recombined in space.

The stretched beam is then seeded into the amplifier. [add final length of the beam] The amplifier is a stable laser cavity whose gain medium is a Ti:sapphire rod pumped by the Evolution laser. Gain saturation is obtained when the pulsed passed the laser rod about twenty times. This is achieved using polarization optics controlled by timing electronics. The seed enters the cavity in the s polarization reflecting off the laser rod at Brewster's angle. An input Pockels cell located between the rod and the first cavity mirror is turned on as soon as the pulse passed it for the first time. From this point, it behaves as a quarter-wave plate. When coupled to the action of an intracavity quarter-wave plate, this rotates the pulse polarization to the p orientation, trapping the pulse in the cavity. Pulse buildup is monitored by a fast photodiode located after one of the

mirrors. After about 20 passes, an exit Pockels cell located close to the other cavity mirror is turned on, rotating the polarization back to the s state, triggering ejection of the pulse by an intracavity polarizing beamsplitter. The amplified pulse is then directed to a compressor, similar in principle to the stretcher, but set up with inverse GVD. The final pulse duration is 100 fs, as measured by a single-shot autocorrelator.

3.3.1.3. Tunability

Tunability was obtained with a Quantronix TOPAS. It is an optical parametric amplifier (OPA) capable of generating pulses from 1.1 μm to 2.6 μm , which can be frequency-doubled down to 550 nm. Pulse energies vary from a few to 100 μJ depending on the wavelength. Optical parametric generation is a second order nonlinear optical phenomenon where two photons, signal and idler, are generated from one pump photon. Conservation of energy states that the sum of the frequencies of the signal and idler is equal to the frequency of the pump. Momentum conservation (or phase-matching condition) states that the vector sum of the signal and idler momenta is equal to the pump's momentum. Since the nonlinear crystal is typically birefringent, it needs to be tuned by rotating it to achieve phase matching. In optical parametric amplification, the crystal is seeded by the signal in presence of the pump, and these result in the generation of the idler and in amplification of the signal. Devices taking advantage of this phenomenon are OPAs and optical parametric oscillators (OPOs). In OPOs, the nonlinear crystal is located in a resonant cavity, so that parametric generation can be obtained from

rather weak pumps. On the other hand, OPAs do not have a cavity, though they require strong pump peak powers, and are therefore easier to align.

The TOPAS is an OPA built around a beta-barium borate (BBO) crystal, which is passed 5 times. The BBO crystal is located on a rotation stage. The first pass is used for superfluorescence generation, which is preamplified in the absence of the pump in the two subsequent passes. The signal frequency is selected with a grating after the third pass, and the last two passes are used for parametric amplification of the signal with the pump. A quartz compensation plate fixed to the same rotation stage as the BBO is used to make up for the displacement of the beam due to BBO rotation. The output of the TOPAS is the sum of a vertically polarized signal pulse with a wavelength from 1.14 μm to 1.6 μm and an horizontally polarized idler pulse with a wavelength between 1.6 μm and 2.6 μm . A second BBO crystal may be used at the TOPAS exit for frequency doubling of the idler or the signal. The pulses are separated using filters.

3.3.2 Pump-probe apparatus description

The pump-probe apparatus is shown on figure 11. After the pulse intensity is attenuated by a neutral density filter, the pump and probe pulses are separated by a plate beamsplitter. The pump beam is reflected towards a fixed delay line while the probe beam was transmitted toward a computer-controlled, motorized, variable delay line. The translation stage was a Micro-Controle MM2000. It has 10 cm travel with a resolution of 5 μm . In this configuration, this translates in a total delay of 666 ps with a resolution of 33 fs. Care was taken during the alignment that the beam was in the delay line's

translational axis. The reflective element was chosen to be a set of two orthogonal mirrors instead of a 90 degree prism for two reasons. First, dispersive elements add unnecessary GVD and therefore create pulse broadening. Second, the separation needed between the incident and backreflected beams was too large for cost-effective prisms. Care was taken as well to set the mirrors in an orthogonal fashion. Proper alignment of the delay line was verified when no deviation in the backreflected beam was observed in the far-field as the stage was moved. A neutral density filter was added after the variable delay line to adjust the pump-to-probe intensity ratio. Both pump and probe pulses were recombined on the second beamsplitter with a separation distance of 4 mm. This was necessary to ensure that the beams were separated on the signal detector. One half of the energy was directed at a detector that served as reference, while another half was directed at a 5 cm focal length lens. The lens focused both pulses on the sample, located near to the focal point. Pump and probe overlap was observed on the screen located at 16 cm of the focal point. Pump and probe overlap was observed on the screen located at 16 cm of an extra microscope objective focused on the sample's front end. The microscope objective was removed after the initial alignment and a detector was placed in the path of the transmitted probe while the pump beam was blocked with a black surface.

The detectors were chosen to be Newport 818-SL. They are large-area silicon photodiodes. Each was connected to a transimpedance amplifier. This circuit allowed the detectors to be used in the photovoltaic mode, that is, with no bias. This ensures that dark current is virtually eliminated, thus keeping shot noise to a minimum. The second function of transimpedance amplifiers is current-to-voltage converters. A capacitor is needed for circuit stability. In order to suppress noise due to undersampling, a first-order

active low-pass filter had to be added after the amplifier to keep the signal's bandwidth below half the acquisition card's sampling rate. The circuits were made with off-the-shelf components available from mainstream electronics stores, and printed on a circuit board. The acquisition card was a National Instrument DAQ.

The software was written in LabView. Its function was to adjust and record experimental parameters, operate the motorized stage, read the acquisition card, perform some digital signal processing (DSP) and statistical analysis at each step, and save the results to a file. The acquisition time was typically 400 to 800 ms, compared to the laser repetition rate of 500 Hz. Therefore, each acquired waveform contained several hundred pulses. The DSP feature had two noise rejection filters, one for high-frequency, and another one for low-frequency noise. The low-frequency rejection filter was used because of lights in the lab that could not be shut off, such as front panel diodes and computer and oscilloscope monitors. The traditional approach that consists in applying a high-pass filter in the frequency domain could not be used here because the pulse-to-pulse variation of the laser is contained in these low frequencies. Instead, advantage was taken from the fact that the pulses actually had a low duty cycle. The software detected pulses, and used the dead time between pulses to calculate a baseline signal, which was then subtracted from the waveform. The second DSP module was a matched filter. Its purpose was to clean the waveforms of electronic noise in the circuit and cables. The pulse shape was recorded prior to the experiment, and the waveform was cross-correlated with this ideal pulse shape. The obtained waveform had a different shape, but that was not a problem since the technique is linear. Peak intensities were then measured for both the signal and reference.

Pulses whose intensities varied by more than a predefined percentage of the median value were discarded. Remaining signal and reference pulses were carefully matched, and the signal-to-reference ratio was calculated for each pulse. Finally, the average value and the standard deviation of the signal, reference and ratio were calculated and written to file.

The software also allowed live monitoring of the ratio average, signal average and reference average plotted as a function of the time delay, as well as the signal and reference waveforms.

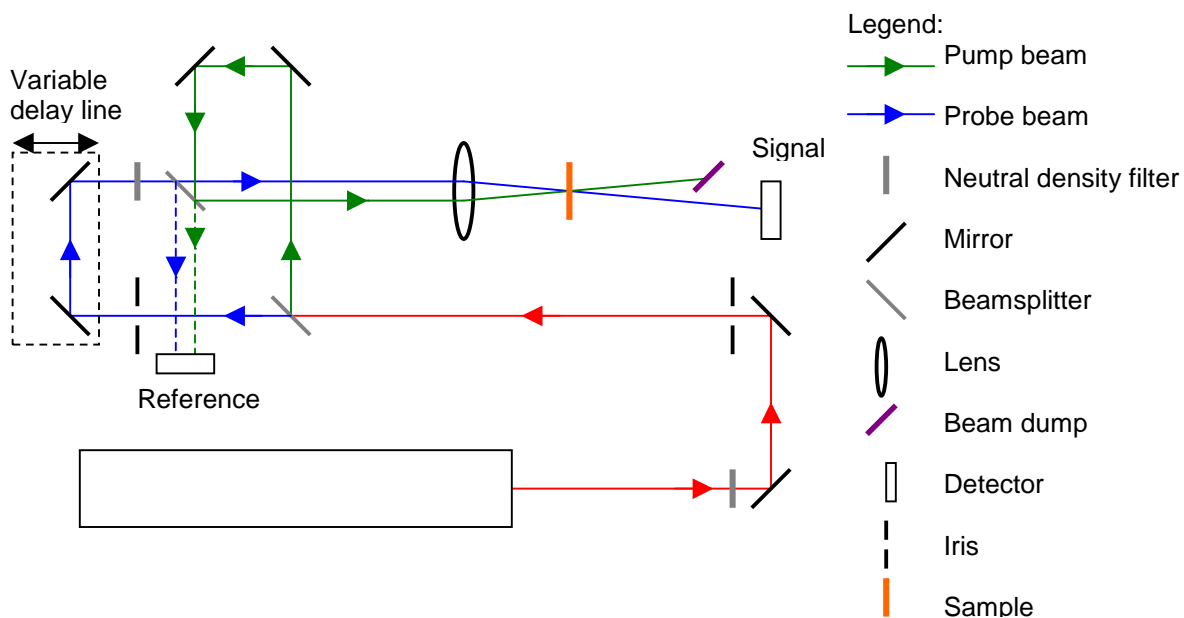


Figure 11: Optical layout of the pump-probe apparatus

3.3.3 Experimental procedure

The Millenia was turned on first and left to warm up for at least 15 minutes as its shutter was closed. The shutter was then opened so the Spitfire could warm up. After 5

minutes, the Spitfire's AOM was turned on to mode-lock the laser. The Evolution was then turned on. After an additional 15 minutes, the Tsunami's central wavelength and bandwidth were checked on the oscilloscope and the Spitfire's input shutters were opened. Both Pockels cells were turned on, and the whole system was left to warm up for another 30 minutes. If the power was sufficient, the TOPAS shutters were opened, and its output energy was checked at 1500 nm. The TOPAS was then tuned to the desired wavelength, and delay stages inside the OPA were adjusted for optimal power if necessary. The OPA's output was blocked and it was left to warm up some more. Meanwhile, the sample was placed on a translation stage whose axis was parallel to the lens optical axis. A collimated white light source was set up to illuminate the sample through the lens. A 40X long working distance microscope objective was set up on the translation stage behind the sample. A screen was placed about 16 cm behind the objective. It was focused on the sample front end by observing a dot written with a thin marker. When this was accomplished, the routing mirrors were adjusted so the beam went through the irises' centers. The pump and probe beams were observed on the screen, and the beamsplitter was adjusted so the pump was aligned on the probe. A proper neutral density filter was then placed in the path of the probe. The microscope objective was removed, and the signal detector was carefully aligned in the probe beam path. An adequate filter was placed in front of both detectors so their peak voltages would be in the same range between 100 mV and 5 V. This was necessary because the acquisition card's gain is the same for both channels. The software was started. Proper gain was chosen, the laser repetition rate, the electronic pulse duty cycle, the acquisition time, the translation

stage speed, step, direction and maximum travel were entered. The pulse shape was recorded and stored for the matched filter.

CHAPTER 4

RESULTS AND DISCUSSION

4.1 Transmission spectroscopy

4.1.1 Calculation of the absorption coefficient of the film

The transmission spectra in the UV to NIR regions of the four samples were normalized with regard to the substrate. The resulting spectra are shown on figures 12 and 13. To distinguish between Fabry-Perot oscillations due to the thickness of the film and actual absorption features from the film, the spectra were fitted in Mathematica to the simple Airy-like model discussed in III.2.1.b. The index of the glass substrate was assumed to follow the dispersion formula for fused silica [114-116] given in the following Sellmeier equation:

$$n_s^2 = 1 + \frac{0.6961663\lambda^2}{\lambda^2 - 0.0684043^2} + \frac{0.4079426\lambda^2}{\lambda^2 - 0.1162414^2} + \frac{0.8974794\lambda^2}{\lambda^2 - 9.896161^2} \quad (4.1)$$

where λ is in microns. The film index was written as:

$$n = n_s (1 + x + y^2 / \lambda^2) \quad (4.2)$$

where x is unitless and y has the unit of the wavelength. This expression has the advantage of limiting the number of fitting parameters to only two constants, and its form recognizes that the dispersion curve shapes are more likely to depart close to the bandgap, that is, at shorter wavelength. It turned out that in the analysis, y could be kept null. Therefore, only two parameters remained: x and the film thickness d .

The strategy for fitting had three steps. In the first step, the fringes in the low absorption NIR region were used to find rough values for d and x . As shown by equation (2.11), the fringe amplitude is proportional to x while the fringe frequency is proportional to $(1+x)d$. Equation (2.8) with no absorption was simply fitted to the measured data. In the second step, the fringe periodicity in the visible region was used to find a better value for $(1+x)d$. The measured transmittance data was smoothed by a moving average algorithm covering five points. Then the second derivative with regards to the wavenumber was calculated. This operation filtered out many of the spectral features while keeping the fringes. The second derivative of equation (2.8) was calculated with an arbitrary absorption coefficient and an arbitrary x , and the fringes were matched by adjusting $(1+x)d$. An example for the first two steps is shown on figure 14. In the last step, equation (2.8) was solved numerically for α for each data point. Each set of data only took 2-3 seconds on a laptop. The derivative $d\alpha/d\tilde{\nu}$ was plotted, and x and $(1+x)d$ were successively adjusted to reduce the amplitude of the remaining fringes until they were reduced to a minimum. Differentiating the absorption coefficient with respect to the wavenumber is convenient because the wavenumber is directly proportional to the photon energy and the result is unitless. Again, the derivative brings out the unwanted interference fringes, making them more detectable. The absorption spectra are shown in figure 15, and the derivatives are shown on figure 16.

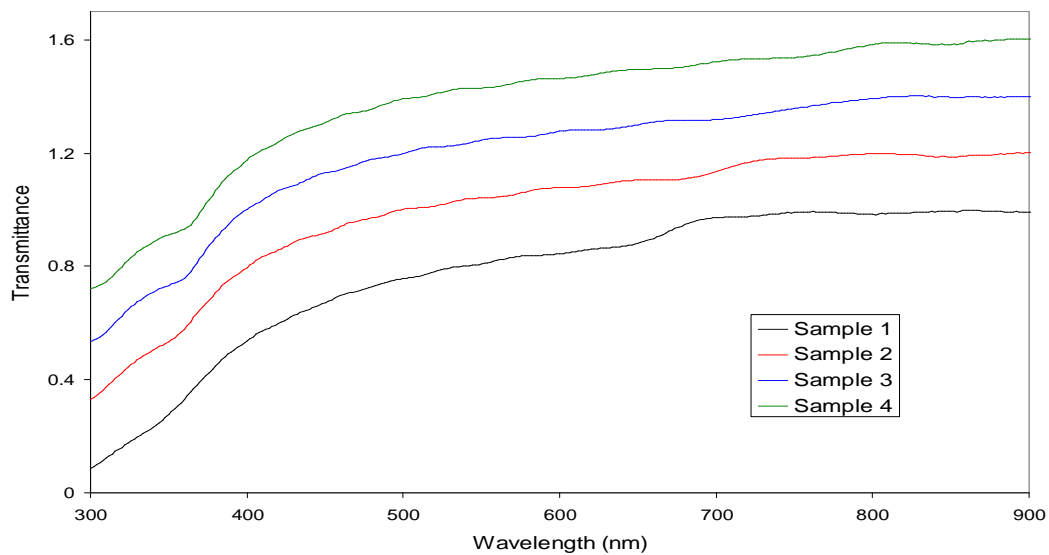


Figure 12: Normalized transmittance of the four samples about the visible. For clarity, the spectra are separated by a constant of 0.2

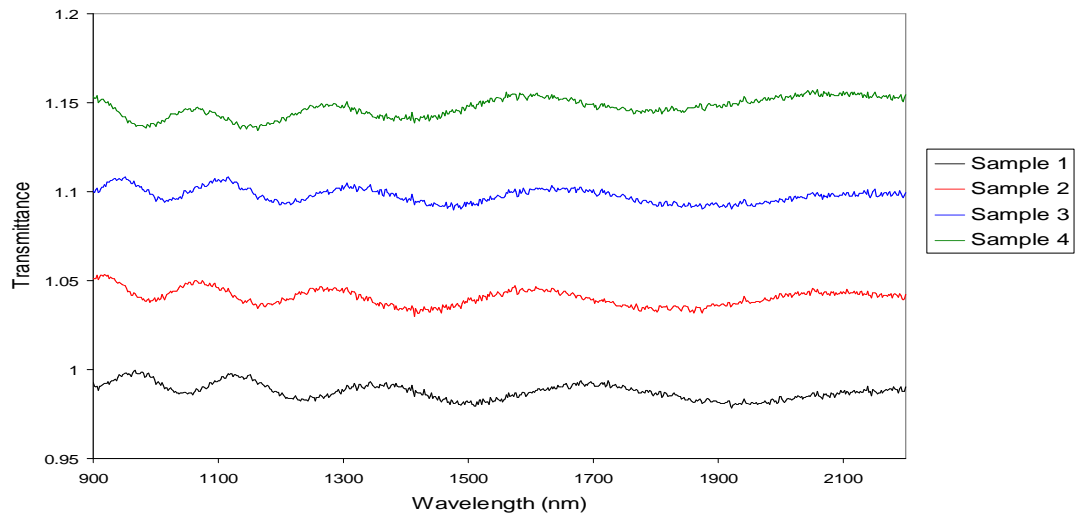
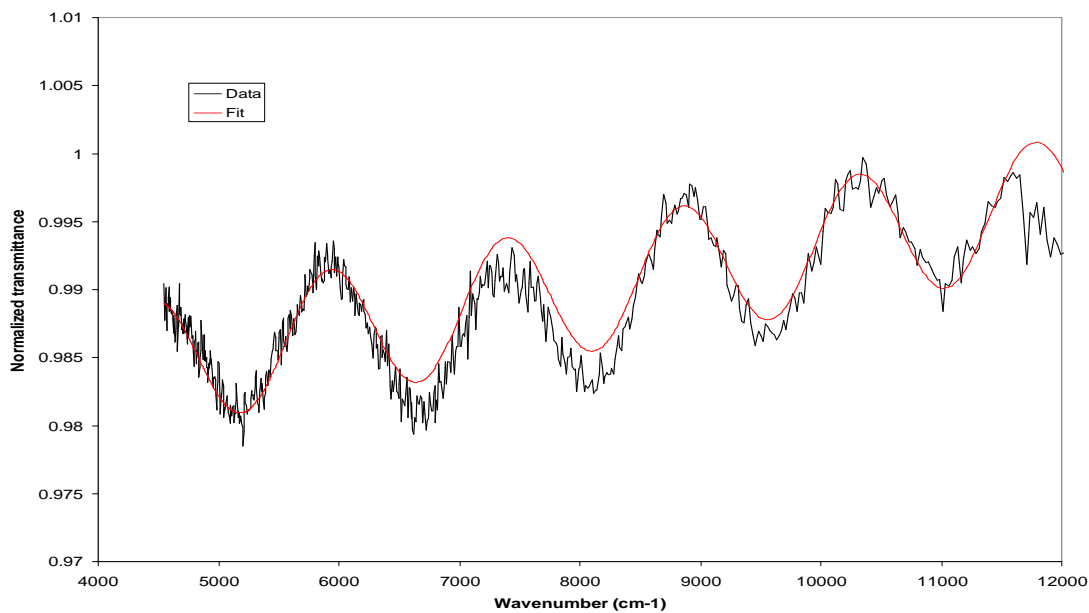


Figure 13: Normalized transmittance of the four samples in the near infrared. For clarity, the spectra are separated by a constant of 0.05

(a)



(b)

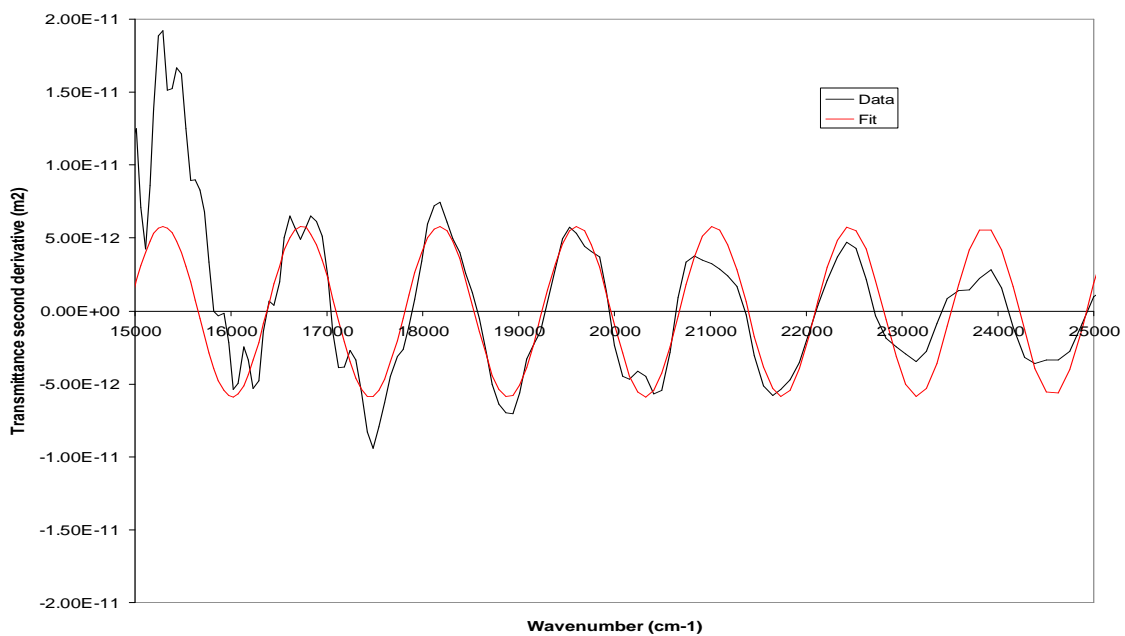


Figure 14: Examples of fitting x and d to the data (a) in the NIR, low absorption region ($x=2.5\%$, $d(1.x)=2.34 \mu\text{m}$, and, (b) in the visible region, using second derivatives ($d(1+x)=2.352 \mu\text{m}$))

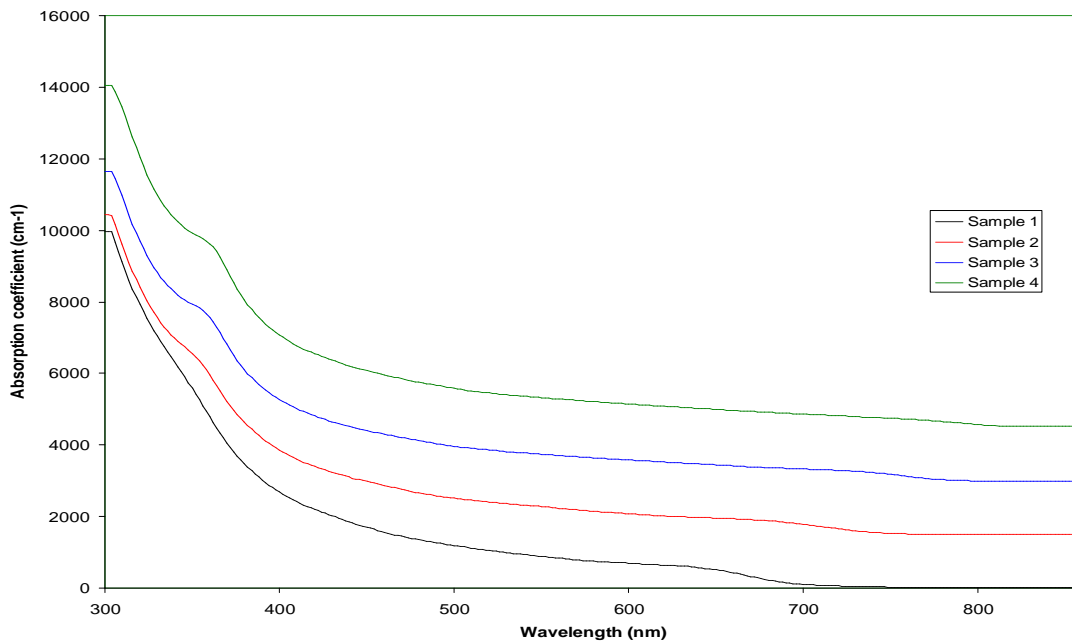


Figure 15: Calculated absorption coefficients of the four films around the visible region. For clarity, the spectra are separated by a constant of 1500 cm^{-1}

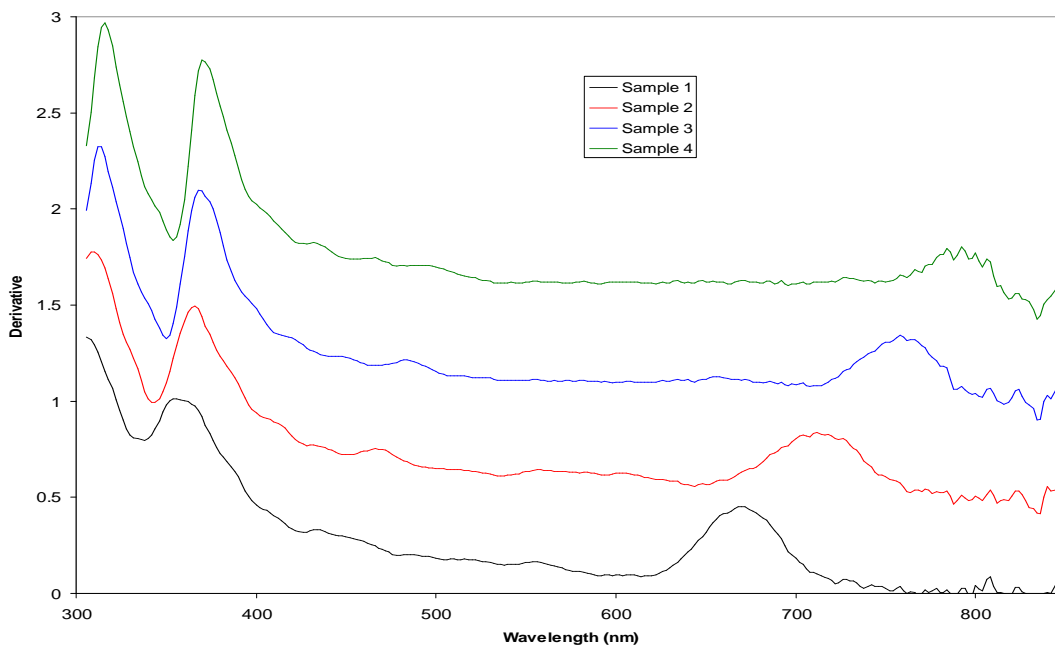


Figure 16: Calculated absorption coefficient derivatives of the four films around the visible region. For clarity, the spectra are separated by a constant of 0.5

4.1.2 Absorption spectrum analysis

Three features clearly appear on the derivative of the absorption coefficient on figure 16. Potter [117] attributed the lowest energy transition to the lowest transition at the Γ -point. It is clear from the graph that, as confinement increases (sample 4 to 1), the transition is shifted to higher energies as expected. Potter defined the transition energy as the maximum of the first derivative of the absorption spectrum. He measured it for a variety of samples of varying average radii. He showed that the transition energy varies as $1/a^2$ for medium-sized QD samples with radii ranging from 2.2 nm to 12 nm. The dependence seems to reach an asymptotic curve for smaller dots. This is due to the non-parabolicity of the bands and to the fact that the QD well has finite barriers. The transition energies measured here however fall in the range of the parabolic approximation. Therefore, one can simply calculate the average dot radius from his best fit linear curve, provided that the same definition of the transition energy is used, that is, the position of the lowest energy extremum in the derivative of the transmission spectrum. The transition energy is related to the average size by the formula:

$$E_{transition} = 1.5342 + \frac{143.8}{a^2} \quad (4.3)$$

where E is in eV and a in Å.

Schmitt-Rink [2] showed that the imaginary part of the electric permittivity of a single quantum dot in the strong confinement regime is inversely proportional to its volume and to the square of the photon energy. The absorption coefficient, on the other hand, is proportional to the product of the photon energy by the imaginary part of the

permittivity.[118] If the homogeneous broadening of the transitions is neglected, the absorption coefficient of a distribution of QDs is therefore:

$$\alpha_1(E) = A \frac{1}{a(E)^3 E} N(a(E)) \quad (4.4)$$

where A is a constant, N(a) is the size distribution, and a(E) is the radius whose confinement energy matches the photon energy, i.e., E is of the form $E = E_G + \gamma/a^2$. This shows that absorption grows stronger with confinement.

To validate the absorption data, the calculated absorption coefficient spectra of samples 1, 2 and 3 were fit to equation 4.4. However, because of the broad size distribution and the overlap of the higher excited states above the bandgap, the absorption coefficient itself carries little information. Fitting its first derivative to the first derivative of equation 4.4 is much more sensitive because it shows sharper features. The size distribution was assumed Gaussian with standard deviation σ_a . Potter's value was used for the bandgap of the bulk, and the average radius was calculated as described in the above paragraph. For each sample, the fitting parameters were A, σ_a and the confinement parameter γ . The energy of the first confined level of the mean radius QD E_0 for each sample was calculated from these parameters. The parameters are listed in table 2 along with the transition energies and calculated average radii. The parameter γ shows little change, indicating that a small correction to the bandgap must be made. The radii standard deviations are growing with heat treatment as expected, and vary from 15% to 40%. Potter measured standard deviations of 20% in TEM of extraction replica.[107] The curve fitting for sample 4 is subject to large errors for several reasons. First, its transition

energy is close to the noisier part of the spectrum where the change of detector occurs in the spectrometer, and the first derivative is even noisier. Second, the size distribution for this sample would be rather large, causing important inhomogeneous broadening. Third, the average dot is large, which means that the higher excited states are close to the first one, and it becomes hard to resolve the first state. However, the spectrum does not contradict the trend seen on figure 17; a point was on the graph, but its margin of error was very large. The results of the curve fitting are shown on figure 18.

The energy of the first level of the mean dot is plotted on figure 17 versus $1/a^2$, along Potter's transition energies and the theoretical prediction by Efros and Rosen [48] based on the 8-parabolic band model. It was fitted to the following equation:

$$E_1 = 1.5404 + \frac{183.25}{a^2} \quad (4.5)$$

where E is in eV and a in Å. The energy of the mean dot is systematically larger than Potter's transition energy because the latter energy is defined as the maximum of the first derivative of the function $N(a(E))/a^3$, whereas the former is the maximum of $N(a(E))$; E_0 cannot be read directly from the absorption spectrum nor its derivative. The deviation between the measured energy and predictions such as Efros's were attributed by Potter to Coulomb interactions.[106]

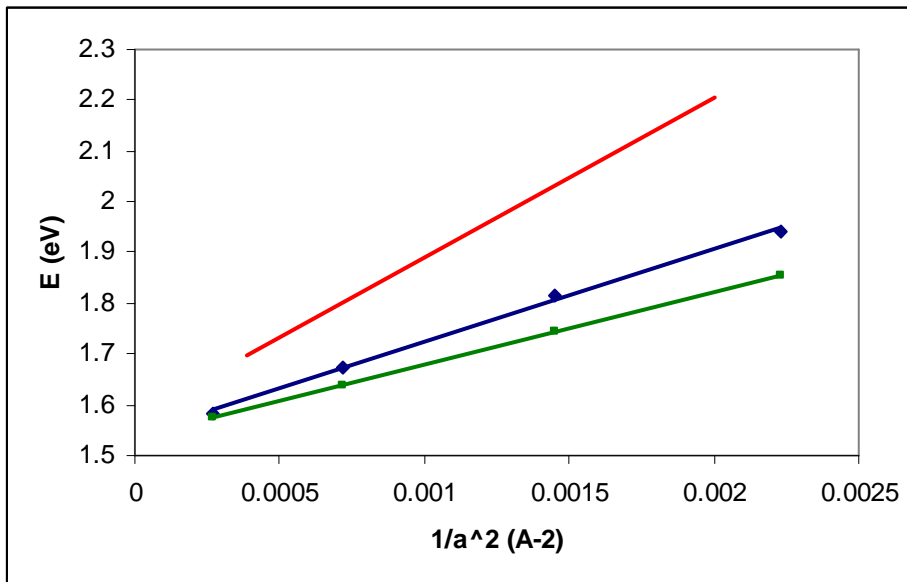


Figure 17: Energy levels. Red: Efros model. Blue: Fitted mean radius energy. Green: Potter's transition energy

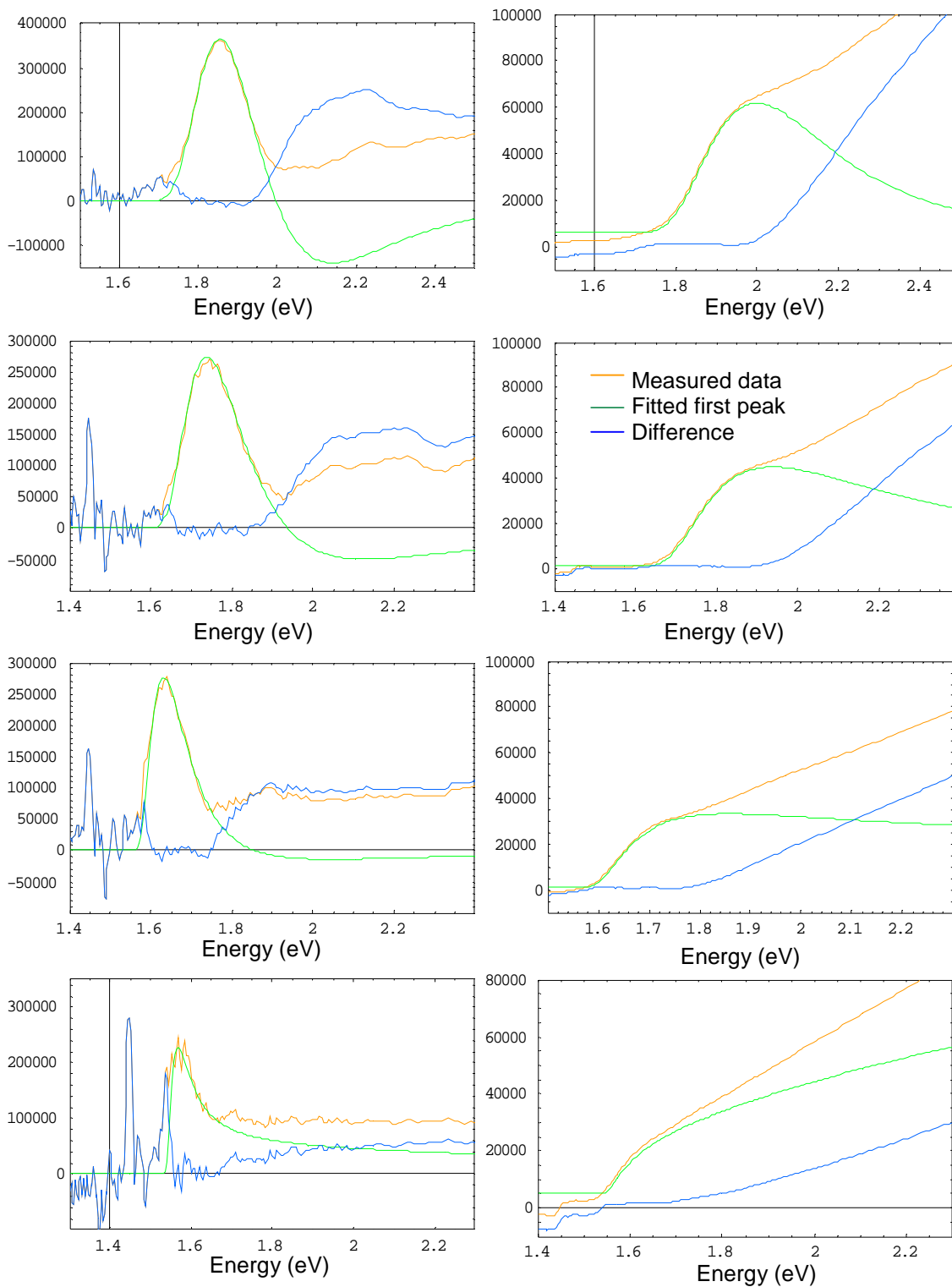


Figure 18: First derivative (left) and absorption coefficient (right) curve fittings. From top to bottom: sample 1 to 4.

4.2 Photoluminescence

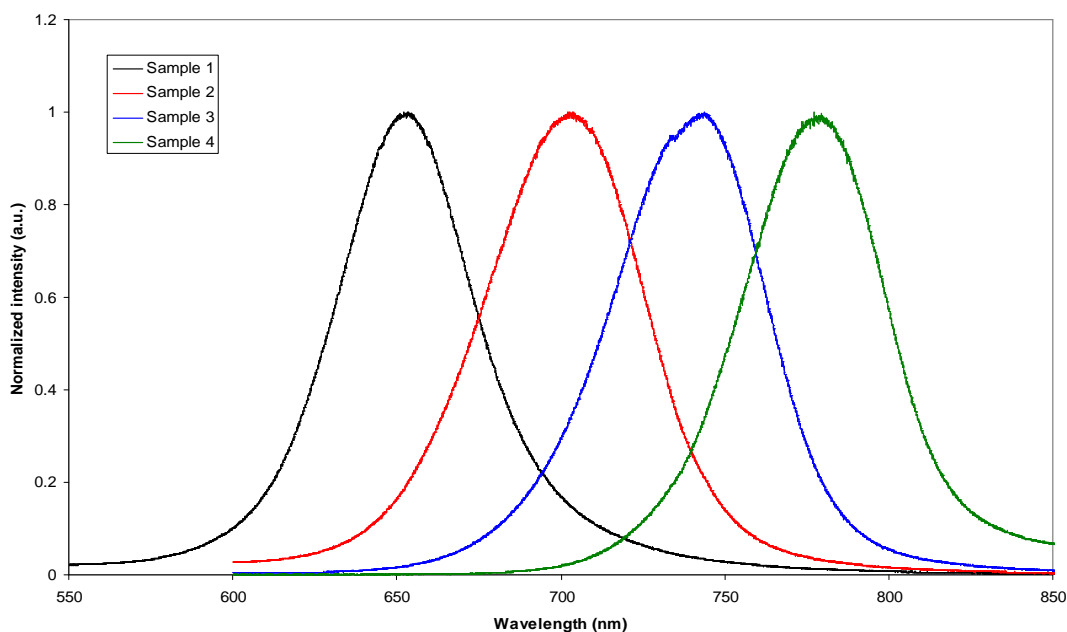


Figure 19: Normalized photoluminescence spectra

The photoluminescence spectra of the four CdTe QD samples are shown on figure 19. Their intensities were adjusted for the peaks to be equal. The excitation source was the 514.5 nm line of an argon ion laser. Peak intensities were showing a slow time decay, with a time constant in the order of tens of seconds. Using the 488 nm line gave similar PL spectra, with a shift of less than 2 nm to the blue for samples 1, 3 and 4. The PL peak of sample 2 was shifted 3 nm to the red. Considering the much larger FWHM of the peaks, the time decay of the intensity, and the fact that each spectrum necessitated several acquisitions to cover the entire spectral range, those shifts are subject to instrumental error. The peak positions show the usual blue shift from sample 4 to 1 due to

confinement. The peaks were recorded until 950 nm, close to the band edge of the instrument's CCD. No long wavelength peak was observed in that range. This indicates a lack of deep traps in the nanoclusters.

Besides a shoulder on the blue side of the peak for sample 3, the peaks appear to be symmetrical, and their shape is a mix between a Lorentzian and a Gaussian curve, suggesting that neither homogeneous nor inhomogeneous broadening is dominant. The symmetry of the peaks shows that not all QDs in each sample participate to the PL process. This is due to the fact that if the size distribution is Gaussian, and therefore symmetrical with respect to the radius, it is not symmetrical with respect to energy, since the energy increases with the inverse square of the radius. The excitation source is spectrally narrow, causing size selection of the quantum dots for the photoluminescence. That is, only the QD whose sizes verify, in first approximation, $E_{\text{excitation}} = E_G + \gamma_i / a^2$, for each transition, are excited, and therefore can relax to the lowest state and radiatively decay from there. This can't explain however why, in particular, sample 4, which contains the largest mean dot and the largest standard deviation of dots, does not have either multiple peaks at higher energies, or a broader overall peak, due to the wide dot size distribution. Absorption in the film would certainly play a role attenuating those higher energy peaks, but the film is thin, and the absorbance is still low, even just above the first transition, thus this cannot explain alone the symmetry of the peak.

The PL peaks are plotted on figure 20 with the calculated absorption coefficients and their contribution to the first transition. The peak is systematically shifted to the red with regards to the band edge absorption and the energy of the mean dot. Ochoa [119]

reported similar red shifts and FWHM for similar CdTe QDs. The Stokes shift is attributable to three different phenomena, none of which however can explain the peak shape. First, Efros [49] pointed out that the excitation probability is proportional to the product of the absorption coefficient and the volume, for excitations far above the band edge. This causes the larger, red-shifted dots to play a more important role in the PL spectrum than in the absorption spectrum. Wider size distributions cause a larger shift. The proposed mechanism in this case being excitation to a high energy level matching the excitation phonon energy, relaxation to the lowest level, and radiative recombination of the electron-hole pair. The second proposed mechanism takes into account the fine structure of the first energy level. The higher sublevels, called bright exciton states, possess most of the oscillator strength, and are responsible for the absorption spectrum, while electron-hole pair recombination occurs through the lower sublevel, dubbed dark exciton. However, the calculated separation between dark and bright exciton levels is 20 meV at most in 2 nm radius CdTe QDs, depending on the shape.[49] Finally, though the role of intrinsic surface states was dismissed by Bawendi, Ochoa [120] observed the presence of tellurium precipitates on the surface of CdTe QDs that were submitted to long heat treatments. These trap states though are expected to quench the photoluminescence though, and the observed PL peak is actually stronger in samples with smaller QDs.

The symmetry of the peak can be attributed to three phenomena. First, as noted above, the dependence on the volume of the PL favors larger dots over smaller ones, diminishing the relative importance of the dots in the tail of the $1/a^2$ distribution. Second,

the Auger effect also quenches PL in smaller dots, as it is proportional to values between $1/a^3$ to $1/a^7$. Finally, phonon broadening must be taken into account at room temperature.

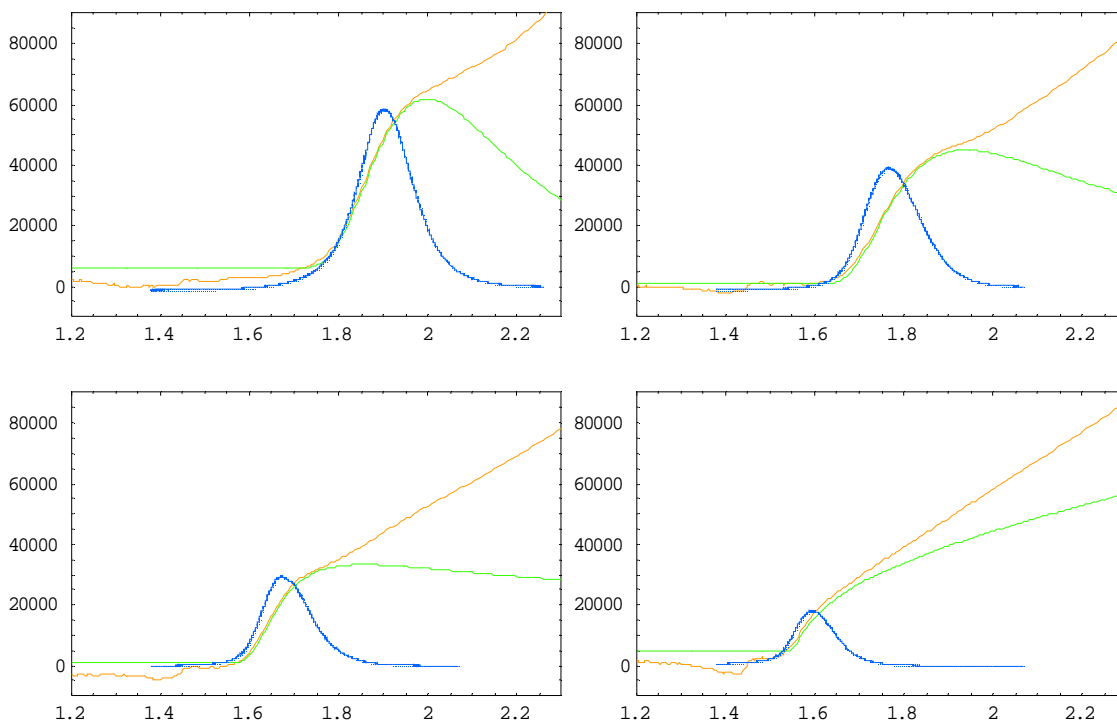


Figure 20: Compared absorption coefficient spectra (orange), contributions of the first transition to the absorption coefficient, and photoluminescence spectra.

Sample	Absorption coefficient first derivative peak position (eV)	Mean radius (Å)	Normalized standard deviation (%)	Fitted mean QD energy (eV)	PL peak position (eV)	PL FWHM (eV)
1	1.855	21.17	15	1.943	1.894	0.144
2	1.743	26.24	23	1.816	1.759	0.144
3	1.637	37.40	29	1.674	1.665	0.124
4	1.573	60.88	40	1.584	1.589	0.105

Table 2: Optical properties of the CdTe samples

4.3 Ultrafast measurements

Pump-probe experiments were first conducted on sample 2 at wavelengths from 670 nm to 740 nm in increments of 10 nm. This allowed the probing of the first excited electron-hole pair of narrow distributions of quantum dots with radii ranging from 24.3 Å to 36.8 Å. The pulse length of about 100 fs translates into an estimated pulse bandwidth of about 10 meV depending on spectral shape, which in turn corresponds to variations in size between 1.6% and 3.5% in the probed QD population. The differential transmission was recorded as a function of the delay. It is written $\Delta T/T_0 = (T(t) - T_0) / T_0$, where $T(t)$ is the transmission of the sample when the probe is incident on the sample with delay t after the pump, and T_0 is the transmission when no pump is applied. For small transmission changes, the differential transmission can be related to the absorption coefficient as follows:

$$\frac{\Delta T(t)}{T_0} = -(\alpha(t) - \alpha_0)\ell \quad (4.6)$$

where ℓ is the sample thickness.

4.3.1 Three-level model

Because the data clearly shows biexponential decay, a simple, three-level model as shown on figure 21 was first used to interpret this data. In this model, the pump initially excites the QDs from the ground state G with population $N_G(t)$ to the excited state B. The carriers may either directly decay from B to G with the recombination rate $R_{B \rightarrow G}$, or to the lower state A with recombination rate $R_{B \rightarrow A}$. QDs in the state A then

decay to the ground state with the recombination rate $R_{A \rightarrow G}$. The absorption coefficient for the probe is then proportional, in first approximation, to the population difference between the ground state and state B. The rate equations for the different energy levels are:

$$\begin{aligned}\frac{dN_B}{dt} &= -\frac{1}{\tau_B} N_B \\ \frac{dN_A}{dt} &= \frac{x}{1+x} \frac{1}{\tau_B} N_B - \frac{1}{\tau_A} N_A \\ \frac{dN_G}{dt} &= \frac{1}{1+x} \frac{1}{\tau_B} N_B + \frac{1}{\tau_A} N_A\end{aligned}\tag{4.7}$$

where τ_B is the overall decay constant from level B, defined as $1/\tau_B = R_{B \rightarrow A} + R_{B \rightarrow G}$, τ_A is the decay time from level A and is defined as $1/\tau_A = R_{A \rightarrow G}$, and x is the ratio between the two recombination rates from level B defined as $x = R_{B \rightarrow A} / R_{B \rightarrow G}$. A large x ratio means that recombination mostly occurs through the intermediate state A, while a small ratio means that electron-hole recombination is mostly a direct process. For simplicity, Auger effects are not taken into account in this model. They will be address in a subsequent paragraph. The absorption coefficient for the E_B - E_G transition is proportional to the population difference between the two levels:

$$\alpha(t) \propto N_G(t) - N_B(t)\tag{4.8}$$

The measured differential transmission curves and their fits are shown on figure 22. The results at 740 nm are not shown because no change in transmission was detected. This is attributed to the low concentration of dots absorbing at that wavelength, the differential transmission signal being lost in the noise. The important noise present in the data is due mainly to poor pulse-to-pulse pointing stability of the optical parametric

amplifier, as qualitatively observed with a CCD camera. The low thickness of the film (about 2 μm) means that relatively few QDs were probed, further diminishing the signal-to-noise ratio.

The fitting parameters τ_A , τ_B , and x are shown in table 3. The fast decay rate τ_A is the initial slope of the differential transmission curve in logarithmic scale, the slower decay rate τ_B is the subsequent slope, and the parameter x weighs the importance of both contributions: a high x means that the slow contribution accounts for a large part of the amplitude of the decay while a small x means that the fast component amounts for most of the decay.

Deep traps seem not to play a role, since no long decay time on the order of hundreds of picoseconds is detected. This correlates with the fact that no broad, long wavelength peak was observed in the photoluminescence spectra. State B, by design of the experiment, corresponds to the $1S_{3/2}(h)$ - $1S(e)$ electron-hole pair. State A may be attributed either to surface states or to a lower sublevel of the fine structure of the first electron-hole pair such as the dark exciton. It is generally attributed to the surface.[121-124]

The initial decay rate τ_B is about 200 fs. Similar subpicosecond decay rates have been observed by others in semiconductor QDs.[121-124] Measurements of the longer decay rate seem to be prone to error due to noise present in the system. It is of the order of several picoseconds. Similar experiments report slower decay rates of the order of tens of picoseconds.[121-124]

The parameter x shows a strong size dependence, and it indicates that electron-hole recombination through the state A is more important for smaller dots than for larger dots. Because smaller dots have a larger surface-to-volume ratio, we attribute A to surface states. However, the dependence of x on the radius is stronger than this ratio (itself proportional to $1/a$), as shown on figure 23. Figure 23 also suggests that the dependence is stronger than $1/a^3$. Again, the controversy about the nature of state A should be outlined. Photoluminescence measurements[63] and studies of gain[6] have been assigning it to the so-called dark exciton.

4.3.2 Considerations about Auger effects

As stated earlier, Klimov [97] did the most careful study of the Auger effect in semiconductor QDs. Since the Auger effect is a nonlinear effect, summation over all QDs in a sample must be done carefully. In first approximation, the first electron-hole pair state is eightfold degenerate,[49] that is, it cannot be populated by more than eight pairs. The decay time $\tau_{A,N}$ when the state is populated by N pairs is proportional $1/N^2$. Therefore, there are up to eight distinct, or “quantized” Auger decay rates for QDs of a given size, depending on the population of the first excited state, with the fastest decay for the most populated QDs, and the slowest decay τ_{A1} on the order of hundreds of picoseconds. Relaxation is shown on figure 21: if, for example, the dot is populated with 4 pairs, the first pair recombines with the time constant τ_{A4} , then the second pair recombines with the time constant τ_{A3} etc. Figure 24 shows the initial population of dots right after pumping depending on the average number of pairs per dot, assuming a Poisson distribution.[97] It demonstrates that the dot initial population is fairly evenly

distributed. The observed decay is the sum of the decays of dots with 1 electron-hole pair, 2 electron-hole pairs, etc. Therefore, it is multiexponential by nature. Because of this cascade decay scheme and the initial dot population, it appears that Auger recombination cannot *alone* explain the biexponential recombination process that we observe, hence the necessity of using the three-level model.

However, because of the high pump intensities used in our measurements, it seems reasonable to assume that Auger effects do take place. Because the Auger constant varies as a^3 , as explained in the background chapter, or even more strongly, the size dependence observed in the three level model can be explained in part by Auger recombination. Unfortunately, the low sensitivity of our experimental apparatus due to relatively high noise cannot resolve multiexponential decays. The experiments were conducted at constant pump intensity though, and population of QDs by multiple pair is likely.

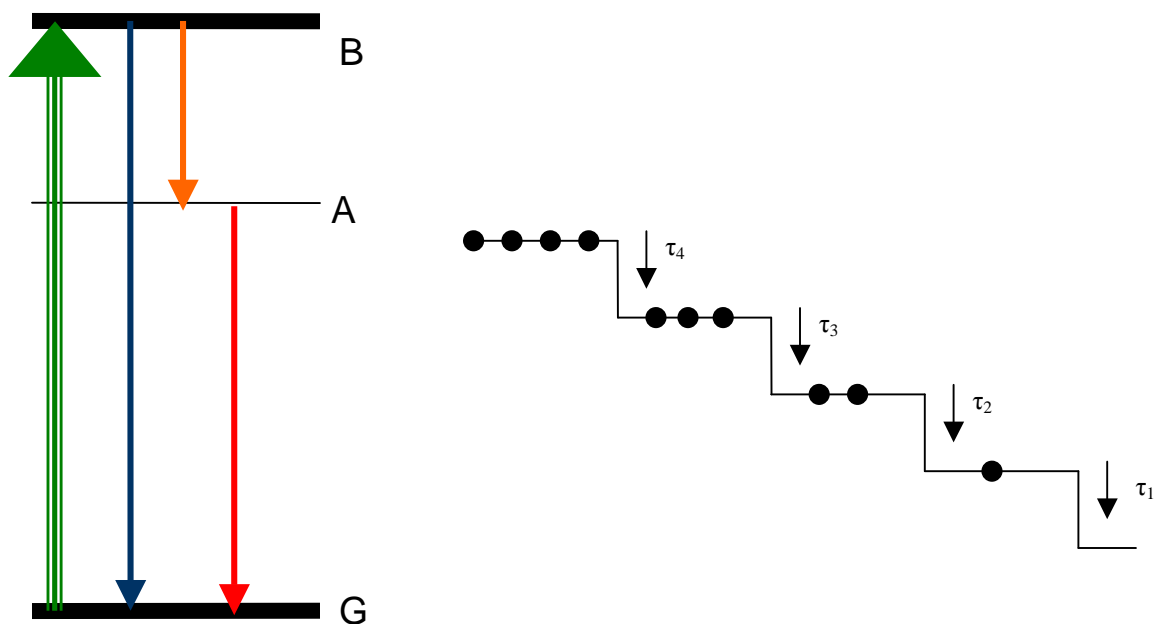
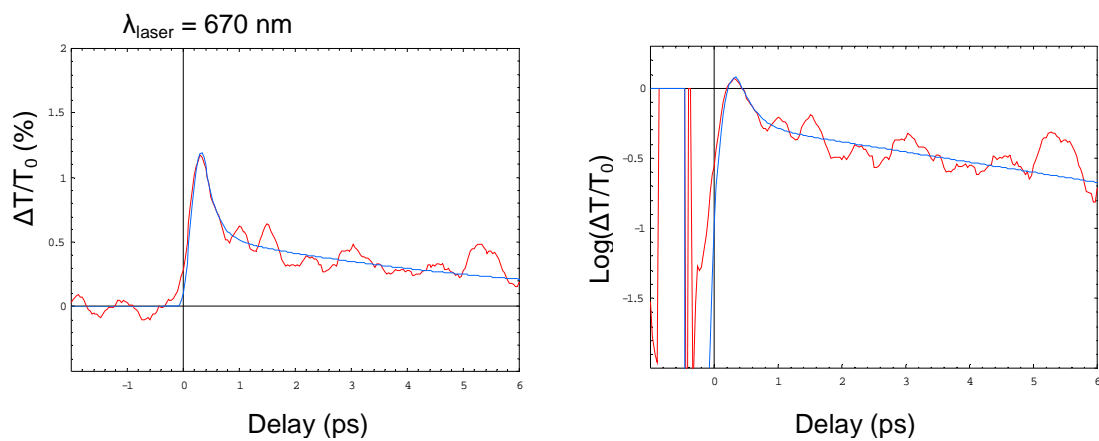
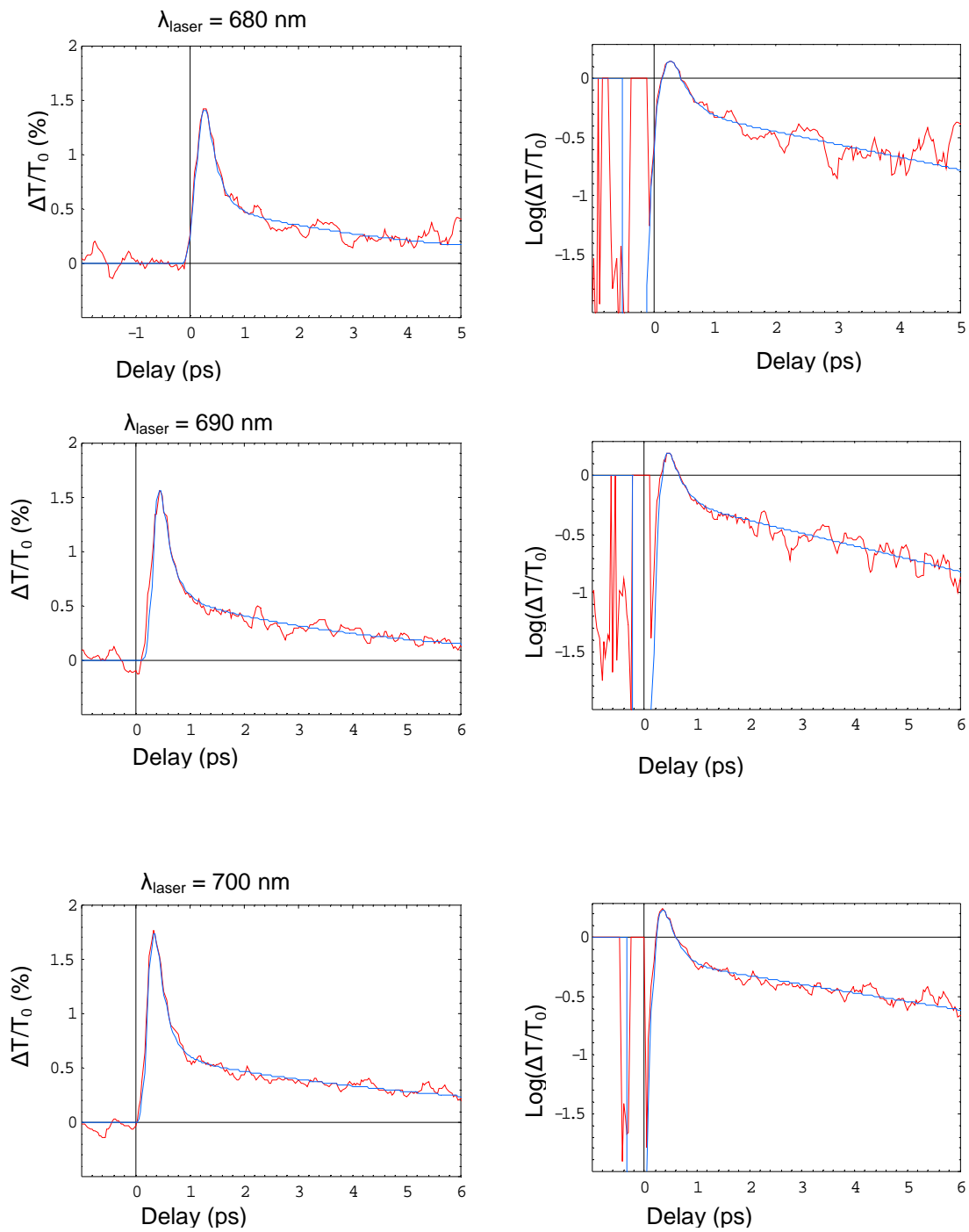


Figure 21: (a) energy diagram for the three-level model; (b) decay scheme for quantized Auger relaxation. Level B can hold as many as eight electrons.





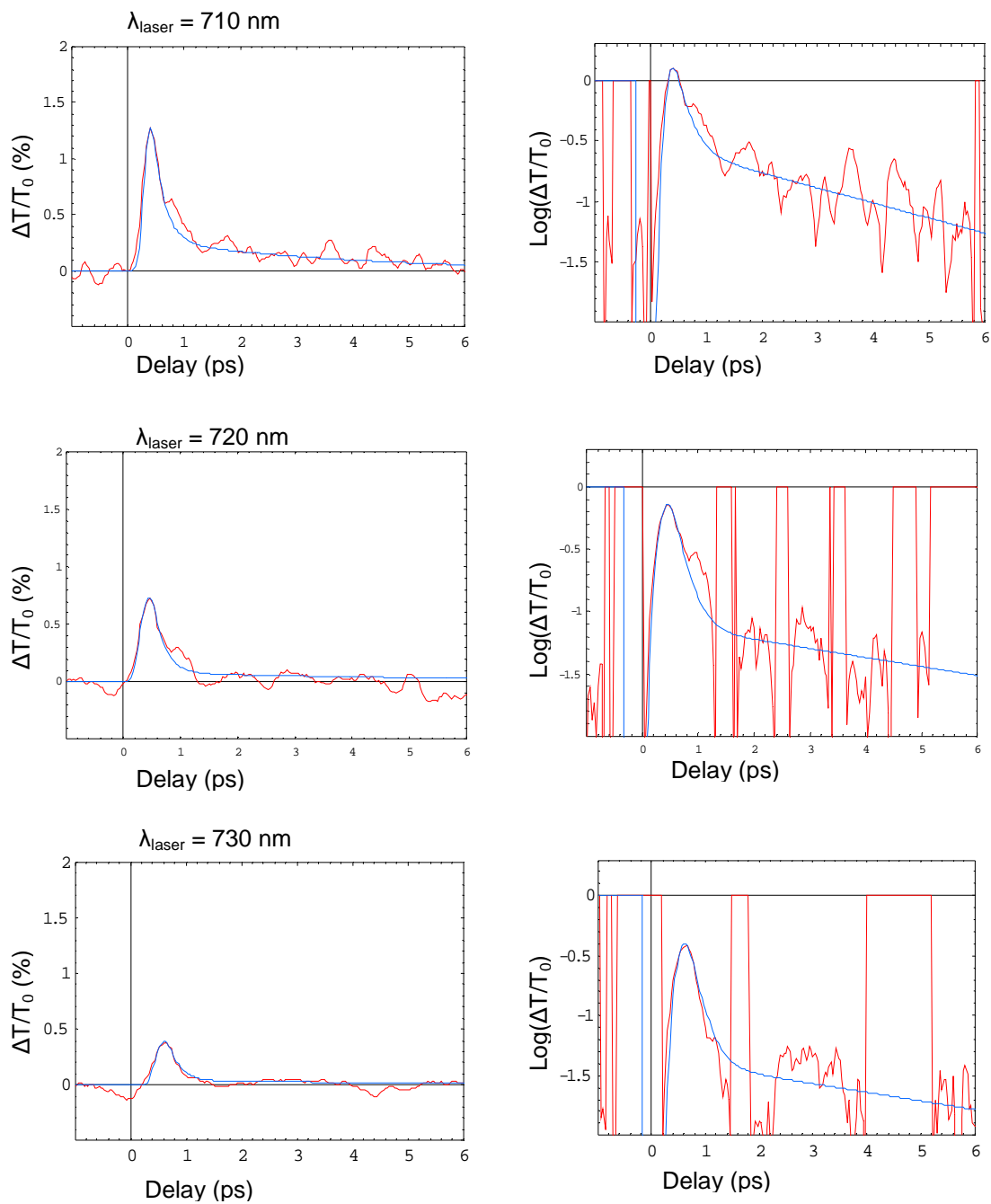


Figure 22: Differential transmission results (red) and curve fits (blue) as a function of delay.

Wavelength (nm)	Energy (eV)	QD radius (Å)	τ_B (ps)	τ_A (ps)	x
670	1.851	24.3	0.2	6.0	1.03
680	1.824	25.4	0.2	4.0	0.67
690	1.797	26.7	0.2	4.0	0.86
700	1.771	28.2	0.2	6.0	0.73
710	1.746	29.8	0.2	3.5	0.30
720	1.772	31.7	0.2	6.0	0.10
730	1.699	34.0	0.2	6.0	0.10
740	1.676	36.8	-----	-----	-----

Table 3: Fitting parameters for the three-level model.

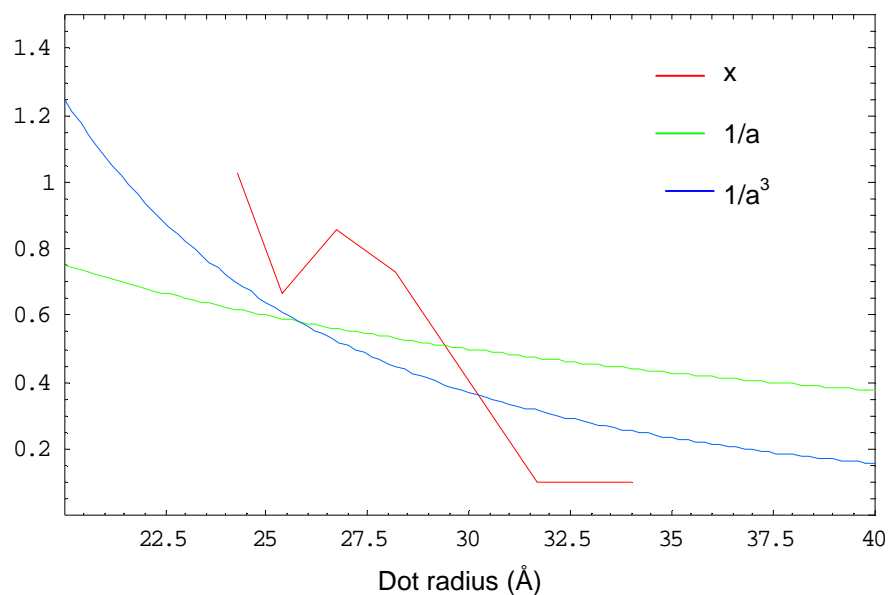


Figure 23: Dot radius dependence of x compared to normalized $1/a$ and $1/a^3$. The error on x is on the order of 10%.

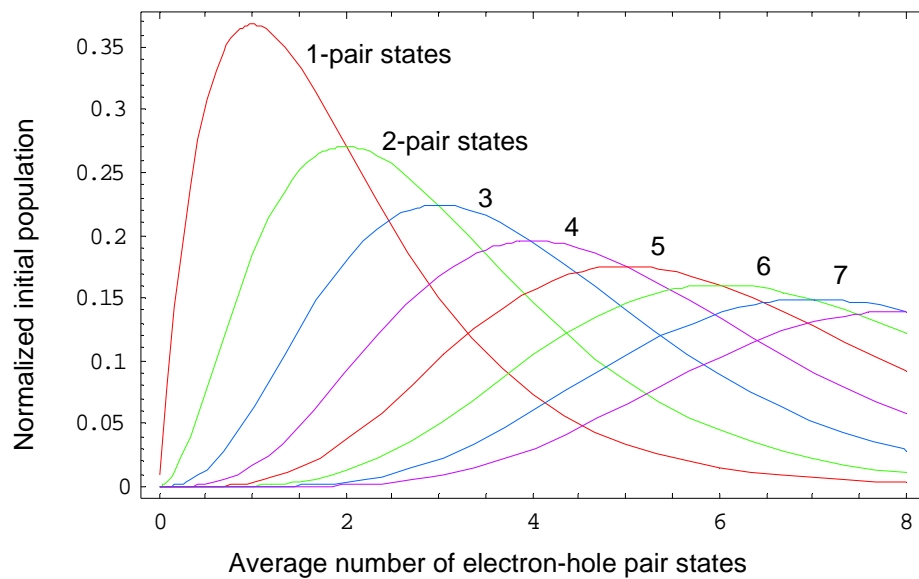


Figure 24: Initial population of 1-pair states, 2-pair states, ..., 8-pair states (from left to right) as a function of the average number of e-h pairs per quantum dot. After [97].

CHAPTER 5

CONCLUSION

This dissertation focused on quantum dots of CdTe made by a sputter-deposition method. The CdTe was fabricated in alternate layers separated by Pyrex glass. The multi-layer films were heat-treated to form quantum dots of various sizes with mean radii of 21 Å, 26 Å, 37 Å and 61 Å, and distribution widths of 15-20%. These sizes are smaller than the exciton Bohr radius (75 Å) for CdTe, placing these quantum dots in the strong confinement regime.

The blue shift of the $1S(e)-1S_{3/2}(h)$ transition due to the confinement of the carriers was observed using transmission spectroscopy. The shift in absorption edge as defined by the maximum in a gaussian peak fitted to the absorbance spectrum follows the $1/a^2$ behavior which has been predicted for both weak and strong confinement regimes. The slope of the $1/a^2$ dependence sits between $1/M$ and $1/\mu$ (where M is the mass of the center of motion of the exciton and μ is the reduced mass) which are predicted for weak and strong confinement respectively. Potter et al. have attributed this behavior to a combination of finite confinement barrier height, size distribution of the quantum dots and mixing of the transition states.

Photoluminescence measurements were conducted on the same set of samples and show bright emission. Quantum efficiency was not measured and remains a good future project. The photoluminescence peak was single but did not have gaussian shape. No red

photoluminescence associated with shallow defects was observed. For each sample, the PL peak was red-shifted from the fitted first absorption peak. The shift decreased with increasing size. It was as high as 49 meV for the sample with the smallest dots, and was undetectable for the sample with the largest dots. In each sample, the photoluminescence peak is assumed to correspond to the $1S(e)-1S_{3/2}(h)$ transition.

The red shift of the photoluminescence peak from the absorption peak may result from a number of causes:

(1) The PL peak may be much broader than the absorption peak and self absorption may reduce the intensity of the emission at shorter wavelengths. However the measured PL peak is well defined and does not exhibit a long tail toward higher energy as expected for this process.

(2) The PL emission may be dominated by the larger quantum dots in the distribution. This process is counter-intuitive since one expects that the larger QD will dominate in the absorption process instead. A calculation of the expected luminescence region based on the assumption of a 20% size distribution width shows that the observed luminescence is red-shifted by an additional 70 meV. It is also expected that the emission cross-section or PL oscillator strength will vary as the product of the volume and the absorption cross-section.

(3) This leaves the postulation of an intermediate, non-absorbing state below the $1S(e)-1S_{3/2}(h)$ transition. This state has been attributed to either intrinsic surface states or a splitting of the $1S(e)-1S_{3/2}(h)$ state into a higher energy absorbing state and a lower energy non-absorbing state. The current measurements could not distinguish between the

two proposed mechanisms. Surface states are important in the solid-state composites and Potter has suggested the formation of a Te-O layer at the QD-glass interface.

Pump-probe measurements were conducted on the sample with the mean dot radius of 26 Å to examine the effect of QD size on carrier recombinations. The pump and probe frequencies were the same. The pump frequency was varied in wavelength to span across both the photoluminescence and the first absorption transition. In all measurements, the decay of transient absorption had two components: a subpicosecond decay followed by a decay of the order of several picoseconds. The very fast transient absorption decay indicates the presence of fast recombination processes in these materials. While sub-picosecond recombination times have been observed in other quantum dots, this is the first observation in thin films CdTe quantum dots. Unfortunately, these measurements do not exclude the presence of long-lived deep traps as the long time tail of the transient absorption decay curve was not studied and is left for future studies.

Again, several potential mechanisms may participate in the observation of two decay times for the transient absorption. These include Auger recombination and a 3-level process in which an intermediate state participates in the photo-excited carrier recombination. The effect of the Auger process was discussed in the paper. The conclusions are that Auger processes must always play a role in carrier recombination. However, since the excited state in CdTe is eight-fold degenerate, the sum of all possible Auger processes results in a broad non-exponential decay curve which is not observed here in the two distinct decay processes. So the Auger process is either a small

component of the recombination process or it occurs outside our time window at longer times.

The biexponential decay behavior can be explained through a 3-state model. The pump excites quantum dots with lowest transition energy matching the pump photon energy, and the probe measures the decay of this transition in those selected quantum dots. The biexponential decay function then indicates that two processes compete in the decay mechanism, one directly to the ground state and one to an intermediate state which is followed to a decay to the ground state. Please note that an intermediate state transition was also required to fit the photoluminescence data.

As mentioned above, the pump frequency for the sample of interest was varied over a range corresponding to the quantum dot size distribution. Thus for each test, a narrow selection of the size distribution was photo-excited. Consequently, comparing the results from these tests allows a study of the effect of quantum dot size on the recombination process. In the analysis of the data we found that fitting the decay curves yields little variation as a variation of QD size for, on one hand the overall decay rate from the excited state, and on the other hand, the decay rate from the intermediate state.

However the curves differed by the decay rate from the excited to the intermediate and ground state. A parameter x was defined as the decay rate from ground to intermediate states divided by the decay rate for the direct recombination from excited to ground states. The data showed that x increases with a decrease in the size of the quantum dots sampled by the pump frequency. This means that transitions to the intermediate state increase in probability in the smaller quantum dots of a size

distribution. Thus the intermediate state plays a stronger role in the recombination process of smaller quantum dots.

An intermediate state between the ground state and first excited state plays a major role in both the PL emission and the photocarrier recombination processes. This is the first paper to our knowledge that analyzes the role of this state in PL and carrier recombination and the first to show that the intermediate state plays a stronger role in smaller quantum dots. Many authors have speculated that surface structure influences the behavior of quantum dots. Surface effects could be responsible for this intermediate state. Clearly the physical nature of this state is important to understanding the dynamics of carriers in strongly confined QDs. This is a critical question for applications of these composite materials in which carrier dynamics play a role, such as in photovoltaics and fluorescence markers.

.

REFERENCES

1. Moriarty, P., *Nanostructured materials*. Reports on Progress in Physics, 2001. **64**(3): p. 297-381.
2. Schmitt-Rink, S., D.A.B. Miller, and D.S. Chemla, *Theory of the Linear and Nonlinear Optical-Properties of Semiconductor Microcrystallites*. Physical Review B, 1987. **35**(15): p. 8113-8125.
3. Bukowski, T.J. and J.H. Simmons, *Quantum dot research: Current state and future prospects*. Critical Reviews in Solid State and Materials Sciences, 2002. **27**(3-4): p. 119-142.
4. Alivisatos, A.P., W.W. Gu, and C. Larabell, *Quantum dots as cellular probes*. Annual Review of Biomedical Engineering, 2005. **7**: p. 55-76.
5. Grundmann, M., *The present status of quantum dot lasers*. Physica E-Low-Dimensional Systems & Nanostructures, 1999. **5**(3): p. 167-184.
6. Klimov, V.I., et al., Optical gain and stimulated emission in nanocrystal quantum dots. Science, 2000. **290**(5490): p. 314-317.
7. Giessen, H., et al., *Femtosecond optical gain in strongly confined quantum dots*. Optics Letters, 1996. **21**(14): p. 1043-1045.
8. Hu, Y.Z., et al., Microscopic theory of optical gain in small semiconductor quantum dots. Physical Review B, 1996. **53**(8): p. 4814-4822.
9. Kershaw, S.V., et al., *Development of IR-emitting colloidal II-VI quantum-dot materials*. Ieee Journal of Selected Topics in Quantum Electronics, 2000. **6**(3): p. 534-543.
10. Liu, Y., et al., *Optical properties of CdTe quantum dots in praseodymium-doped borosilicate glass*. Journal of Materials Science Letters, 1996. **15**(21): p. 1875-1878.
11. Padilha, L.A., et al., *Ultrafast optical switching with CdTe nanocrystals in a glass matrix*. Applied Physics Letters, 2005. **86**(16): p. -.
12. Padilha, L.A., et al., *Two-photon absorption in CdTe quantum dots*. Optics Express, 2005. **13**(17): p. 6460-6467.

13. Padilha, L.A., et al., Frequency degenerate and nondegenerate two-photon absorption spectra of semiconductor quantum dots. *Physical Review B*, 2007. **75**(7): p. -.
14. Madelung, O., W.V.d. Osten, and U. Rossler, eds. *Crystal and solid state physics. Semiconductors. Intrinsic properties of group IV elements and III-V, II-VI and I-VII compounds*. LANDOLT-BORNSTEIN Numerical data and functional relationships in science and technology, ed. O. Madelung. Vol. III/22a. 1987, Springer-Verlag: Berlin.
15. Ebina, A. and T. Takahashi, *Studies of Clean and Adatom Treated Surfaces of II-VI-Compounds*. *Journal of Crystal Growth*, 1982. **59**(1-2): p. 51-64.
16. Rowe, J.M., et al., *Lattice-Dynamics of Cadmium Telluride*. *Physical Review B*, 1974. **10**(2): p. 671-675.
17. Mei, J.R. and V. Lemos, *Photoluminescence on Cdse and Cdte under Hydrostatic-Pressure*. *Solid State Communications*, 1984. **52**(9): p. 785-788.
18. Peyghambarian, N., S.W. Koch, and A. Mysyrowicz, *Introduction to semiconductor optics*. Prentice Hall Series in Solid State Physical Electronics, ed. N.J. Holonyak. 1993, Englewood Cliffs, NJ 07632: Prentice Hall.
19. Haug, H. and S.W. Koch, *Quantum theory of the optical and electronic properties of semiconductors*. Second edition ed. 1993, New Jersey: World Scientific.
20. Yu, P.Y. and M. Cardona, *Fundamentals of semiconductors : physics and materials properties*. 2nd updated ed. 1999, Berlin ; New York: Springer. xvi, 620 p.
21. Kittel, C., *Introduction to solid state physics*. 8th ed. 2005, Hoboken, NJ: Wiley. xix, 680 p.
22. Knox, R.S., *Theory of excitons*. 1963, New York,: Academic Press. vii, 207 p.
23. Chelikowsky, J.R. and M.L. Cohen, Nonlocal Pseudopotential Calculations for Electronic-Structure of 11 Diamond and Zinblende Semiconductors. *Physical Review B*, 1976. **14**(2): p. 556-582.
24. Czyzyk, M.T. and M. Podgorny, Energy-Bands and Optical-Properties of Hgte and Cdte Calculated on the Basis of the Tight-Binding Model with Spin-Orbit Interaction. *Physica Status Solidi B-Basic Research*, 1980. **98**(2): p. 507-516.
25. Nawrocki, M. and A. Twardowski, *Oscillatory Magnetoabsorption in Cdte*. *Physica Status Solidi B-Basic Research*, 1980. **97**(1): p. K61-K64.

26. Sobolev, V.V., O.G. Maksimova, and S.G. Kroitoru, *Reflectivity Spectra and Band-Structure of the ZnTe-CdTe System*. Physica Status Solidi B-Basic Research, 1981. **103**(2): p. 499-509.
27. Romestain, R. and C. Weisbuch, *Optical-Detection of Cyclotron-Resonance in Semiconductors*. Physical Review Letters, 1980. **45**(25): p. 2067-2070.
28. Dang, L.S., G. Neu, and R. Romestain, *Optical-Detection of Cyclotron-Resonance of Electron and Holes in CdTe*. Solid State Communications, 1982. **44**(8): p. 1187-1190.
29. Rossler, U. and H.R. Trebin, *Exchange and Polaron Corrections for Excitons in the Degenerate-Band Case*. Physical Review B, 1981. **23**(4): p. 1961-1970.
30. Efros, A.L. and A.L. Efros, *Interband Absorption of Light in a Semiconductor Sphere*. Soviet Physics Semiconductors-Ussr, 1982. **16**(7): p. 772-775.
31. Efros, A.L. and M. Rosen, *The electronic structure of semiconductor nanocrystals*. Annual Review of Materials Science, 2000. **30**: p. 475-521.
32. Lefebvre, P., et al., *Optical-Properties of II-VI Semiconductor Nanocrystals Produced by Sol-Gel Synthesis in Sodium Borosilicate Glasses*. Superlattices and Microstructures, 1994. **15**(4): p. 447-451.
33. Ekimov, A.I., A.L. Efros, and A.A. Onushchenko, *Quantum Size Effect in Semiconductor Microcrystals*. Solid State Communications, 1985. **56**(11): p. 921-924.
34. Lippens, P.E. and M. Lannoo, *Calculation of the Band-Gap for Small Cds and Zns Crystallites*. Physical Review B, 1989. **39**(15): p. 10935-10942.
35. Sapra, S. and D.D. Sarma, *Evolution of the electronic structure with size in II-VI semiconductor nanocrystals*. Physical Review B, 2004. **69**(12): p. -.
36. Xia, J.-B., *Electronic structures of zero-dimensional quantum wells* Physical Review B, 1989. **40**: p. 8500-8507.
37. Baldereschi, A. and N.O. Lipari, *Spherical Model of Shallow Acceptor States in Semiconductors*. Physical Review B, 1973. **8**(6): p. 2697-2709.
38. Baldereschi, A. and N.O. Lipari, *Cubic Contributions to Spherical Model of Shallow Acceptor States*. Physical Review B, 1974. **9**(4): p. 1525-1539.
39. Koch, S.W., et al., *Coulomb Effects and Optical-Properties of Semiconductor Quantum Dots*. Journal of Crystal Growth, 1992. **117**(1-4): p. 592-597.

40. Sercel, P.C. and K.J. Vahala, Analytical Formalism for Determining Quantum-Wire and Quantum-Dot Band-Structure in the Multiband Envelope-Function Approximation. *Physical Review B*, 1990. **42**(6): p. 3690-3710.
41. Efros, A.L. and A.V. Rodina, *Band-Edge Absorption and Luminescence of Nonspherical Nanometer-Size Crystals*. *Physical Review B*, 1993. **47**(15): p. 10005-10007.
42. Ekimov, A.I., et al., Absorption and Intensity-Dependent Photoluminescence Measurements on Cdse Quantum Dots - Assignment of the 1st Electronic-Transitions. *Journal of the Optical Society of America B-Optical Physics*, 1993. **10**(1): p. 100-107.
43. Richard, T., et al., Effects of finite spin-orbit splitting on optical properties of spherical semiconductor quantum dots. *Physical Review B*, 1996. **53**(11): p. 7287-7298.
44. Lefebvre, P., et al., Influence of spin-orbit split-off band on optical properties of spherical semiconductor nanocrystals. The case of CdTe. *Solid State Communications*, 1996. **98**(4): p. 303-306.
45. Masumoto, Y. and K. Sonobe, *Size-dependent energy levels of CdTe quantum dots*. *Physical Review B*, 1997. **56**(15): p. 9734-9737.
46. Bawendi, M.G., et al., Electronic-Structure and Photoexcited-Carrier Dynamics in Nanometer-Size Cdse Clusters. *Physical Review Letters*, 1990. **65**(13): p. 1623-1626.
47. Dayal, P.B., B.R. Mehta, and P.D. Paulson, Spin-orbit splitting and critical point energy at Gamma and L points of cubic CdTe nanoparticles: Effect of size and nonspherical shape. *Physical Review B*, 2005. **72**(11): p. -.
48. Efros, A.L. and M. Rosen, Quantum size level structure of narrow-gap semiconductor nanocrystals: Effect of band coupling. *Physical Review B*, 1998. **58**(11): p. 7120-7135.
49. Efros, A.L., et al., Band-edge exciton in quantum dots of semiconductors with a degenerate valence band: Dark and bright exciton states. *Physical Review B*, 1996. **54**(7): p. 4843-4856.
50. Brus, L.E., A Simple-Model for the Ionization-Potential, Electron-Affinity, and Aqueous Redox Potentials of Small Semiconductor Crystallites. *Journal of Chemical Physics*, 1983. **79**(11): p. 5566-5571.
51. Hu, Y.Z., M. Lindberg, and S.W. Koch, *Theory of Optically-Excited Intrinsic Semiconductor Quantum Dots*. *Physical Review B*, 1990. **42**(3): p. 1713-1723.

52. Efros, A.L. and A.V. Rodina, *Confined Excitons, Trions and Biexcitons in Semiconductor Microcrystals*. Solid State Communications, 1989. **72**(7): p. 645-649.
53. Takagahara, T., Biexciton States in Semiconductor Quantum Dots and Their Nonlinear Optical-Properties. Physical Review B, 1989. **39**(14): p. 10206-10231.
54. Hu, Y.Z., et al., *Theoretical and Experimental Results on Coulomb Effects in Semiconductor Quantum Dots*. Physica Status Solidi B-Basic Research, 1990. **159**(1): p. 249-257.
55. Esch, V., et al., State Filling, Coulomb, and Trapping Effects in the Optical Nonlinearity of Cdte Quantum Dots in Glass. Physical Review B, 1990. **42**(12): p. 7450-7453.
56. Hu, Y.Z., et al., *Biexcitons in Semiconductor Quantum Dots*. Physical Review Letters, 1990. **64**(15): p. 1805-1807.
57. Park, S.H., et al., *Nonlinear Optical-Properties of Quantum-Confined Cdse Microcrystallites*. Journal of the Optical Society of America B-Optical Physics, 1990. **7**(10): p. 2097-2105.
58. Peyghambarian, N., et al., *Femtosecond Optical Nonlinearities of Cdse Quantum Dots*. Ieee Journal of Quantum Electronics, 1989. **25**(12): p. 2516-2522.
59. Fluegel, B., et al., *Ultrafast Optical Nonlinearities in Ii-Vi Compounds*. Journal of Crystal Growth, 1990. **101**(1-4): p. 643-649.
60. Hu, Y.Z., S.W. Koch, and N. Peyghambarian, *Strongly confined semiconductor quantum dots: Pair excitations and optical properties*. Journal of Luminescence, 1996. **70**: p. 185-202.
61. Kang, K.I., et al., Confinement-Enhanced Biexciton Binding-Energy in Semiconductor Quantum Dots. Physical Review B, 1993. **48**(20): p. 15449-15452.
62. Kang, K.I., et al., Confinement-Induced Valence-Band Mixing in Cds Quantum Dots Observed by 2-Photon Spectroscopy. Physical Review B, 1992. **45**(7): p. 3465-3468.
63. Norris, D.J., et al., *Size dependence of exciton fine structure in CdSe quantum dots*. Physical Review B, 1996. **53**(24): p. 16347-16354.
64. Efros, A.L., *Luminescence Polarization of Cdse Microcrystals*. Physical Review B, 1992. **46**(12): p. 7448-7458.

65. Takagahara, T., Effects of Dielectric Confinement and Electron-Hole Exchange Interaction on Excitonic States in Semiconductor Quantum Dots. *Physical Review B*, 1993. **47**(8): p. 4569-4585.
66. Nirmal, M., et al., *Observation of the Dark Exciton in Cdse Quantum Dots*. *Physical Review Letters*, 1995. **75**(20): p. 3728-3731.
67. Chamarro, M., et al., Enhancement of electron-hole exchange interaction in CdSe nanocrystals: A quantum confinement effect. *Physical Review B*, 1996. **53**(3): p. 1336-1342.
68. Warnock, J., et al., Photoluminescence of Cd1-Xmnxte-Cdte Multiple-Quantum-Well Structures and Superlattices in a Magnetic-Field. *Physical Review B*, 1985. **32**(12): p. 8116-8125.
69. Wang, Y.R. and C.B. Duke, Cleavage Faces of Wurtzite Cds and Cdse - Surface Relaxation and Electronic-Structure. *Physical Review B*, 1988. **37**(11): p. 6417-6424.
70. Bawendi, M.G., et al., Luminescence Properties of Cdse Quantum Crystallites - Resonance between Interior and Surface Localized States. *Journal of Chemical Physics*, 1992. **96**(2): p. 946-954.
71. Bawendi, M.G., et al., *X-Ray Structural Characterization of Larger Cdse Semiconductor Clusters*. *Journal of Chemical Physics*, 1989. **91**(11): p. 7282-7290.
72. Alivisatos, A.P., et al., Electronic States of Semiconductor Clusters - Homogeneous and Inhomogeneous Broadening of the Optical-Spectrum. *Journal of Chemical Physics*, 1988. **89**(7): p. 4001-4011.
73. Hache, F., et al., Photoluminescence Study of Schott Commercial and Experimental Cdse-Doped Glasses - Observation of Surface-States. *Journal of the Optical Society of America B-Optical Physics*, 1991. **8**(9): p. 1802-1806.
74. Norris, D.J. and M.G. Bawendi, *Structure in the Lowest Absorption Feature of Cdse Quantum Dots*. *Journal of Chemical Physics*, 1995. **103**(13): p. 5260-5268.
75. Kuno, M., et al., The band edge luminescence of surface modified CdSe nanocrystallites: Probing the luminescing state. *Journal of Chemical Physics*, 1997. **106**(23): p. 9869-9882.
76. Maly, P., et al., Dominant role of surface states in photoexcited carrier dynamics in CdSe nanocrystalline films prepared by chemical deposition. *Applied Physics Letters*, 2000. **77**(15): p. 2352-2354.

77. Rogach, A.L., Nanocrystalline CdTe and CdTe(S) particles: wet chemical preparation, size-dependent optical properties and perspectives of optoelectronic applications. *Materials Science and Engineering B-Solid State Materials for Advanced Technology*, 2000. **69**: p. 435-440.
78. Borchert, H., et al., Relations between the photoluminescence efficiency of CdTe nanocrystals and their surface properties revealed by synchrotron XPS. *Journal of Physical Chemistry B*, 2003. **107**(36): p. 9662-9668.
79. Liu, Y., et al., *Trap Elimination in Cdte Quantum Dots in Glasses*. *Journal of Materials Science Letters*, 1995. **14**(9): p. 635-639.
80. Kang, K., et al., Room-Temperature Spectral Hole-Burning and Elimination of Photodarkening in Sol-Gel Derived Cds Quantum Dots. *Applied Physics Letters*, 1994. **64**(12): p. 1487-1489.
81. Klimov, V.I. and D.W. McBranch, *Femtosecond IP-to-IS electron relaxation in strongly confined semiconductor nanocrystals*. *Physical Review Letters*, 1998. **80**(18): p. 4028-4031.
82. Klimov, V.I., et al., *Electron and hole relaxation pathways in semiconductor quantum dots*. *Physical Review B*, 1999. **60**(19): p. 13740-13749.
83. Klimov, V.I., et al., Ultrafast dynamics of inter- and intraband transitions in semiconductor nanocrystals: Implications for quantum-dot lasers. *Physical Review B*, 1999. **60**(4): p. R2177-R2180.
84. Poles, E., et al., *Anti-Stokes photoluminescence in colloidal semiconductor quantum dots*. *Applied Physics Letters*, 1999. **75**(7): p. 971-973.
85. Rakovich, Y.P., et al., *Anti-Stokes photoluminescence in II-VI colloidal nanocrystals*. *Physica Status Solidi B-Basic Research*, 2002. **229**(1): p. 449-452.
86. Wang, X.Y., et al., *Photoluminescence upconversion in colloidal CdTe quantum dots*. *Physical Review B*, 2003. **68**(12): p. -.
87. Klimov, V., P.H. Bolivar, and H. Kurz, *Ultrafast carrier dynamics in semiconductor quantum dots*. *Physical Review B*, 1996. **53**(3): p. 1463-1467.
88. Huang, K. and A. Rhys, *Theory of Light Absorption and Non-Radiative Transitions in F-Centres*. *Proceedings of the Royal Society of London Series a-Mathematical and Physical Sciences*, 1950. **204**(1078): p. 406-423.

89. Duke, C.B. and G.D. Mahan, *Phonon-Broadened Impurity Spectra .I. Density of States*. Physical Review, 1965. **139**(6A): p. 1965-&.
90. Prabhu, S.S., et al., *Nonequilibrium Dynamics of Hot Carriers and Hot Phonons in Cdse and Gaas*. Physical Review B, 1995. **51**(20): p. 14233-14246.
91. Klimov, V., P.H. Bolivar, and H. Kurz, *Hot-Phonon Effects in Femtosecond Luminescence Spectra of Electron-Hole Plasmas in Cds*. Physical Review B, 1995. **52**(7): p. 4728-4731.
92. Bockelmann, U. and G. Bastard, *Phonon-Scattering and Energy Relaxation in 2-Dimensional, One-Dimensional, and Zero-Dimensional Electron Gases*. Physical Review B, 1990. **42**(14): p. 8947-8951.
93. Benisty, H., C.M. Sotomayortorres, and C. Weisbuch, *Intrinsic Mechanism for the Poor Luminescence Properties of Quantum-Box Systems*. Physical Review B, 1991. **44**(19): p. 10945-10948.
94. Xu, S., et al., *Hole intraband relaxation in strongly confined quantum dots: Revisiting the "phonon bottleneck" problem*. Physical Review B, 2002. **65**(4): p. -.
95. Efros, A., *Auger Processes in Nanosize Semiconductor Crystals*, in *Semiconductor Nanocrystals: From Basic Principles to Applications*, A. Efros, D.J. Lockwood, and L. Tsybeskov, Editors. 2003, Springer. p. 52-72.
96. Klimov, V.I. and D.W. McBranch, *Auger-process-induced charge separation in semiconductor nanocrystals*. Physical Review B, 1997. **55**(19): p. 13173-13179.
97. Klimov, V.I., et al., *Quantization of multiparticle Auger rates in semiconductor quantum dots*. Science, 2000. **287**(5455): p. 1011-1013.
98. Roussignol, P., et al., *Optical-Phase Conjugation in Semiconductor-Doped Glasses*. Optics Communications, 1985. **55**(2): p. 143-148.
99. Chepic, D.I., et al., *Auger Ionization of Semiconductor Quantum Drops in a Glass Matrix*. Journal of Luminescence, 1990. **47**(3): p. 113-127.
100. Efros, A.L., V.A. Kharchenko, and M. Rosen, *Breaking the Phonon Bottleneck in Nanometer Quantum Dots - Role of Auger-Like Processes*. Solid State Communications, 1995. **93**(4): p. 281-284.
101. Kharchenko, V.A. and M. Rosen, *Auger relaxation processes in semiconductor nanocrystals and quantum wells*. Journal of Luminescence, 1996. **70**: p. 158-169.

102. Blakemore, J.S., *Semiconductor statistics*. 1962, Oxford, New York,: Pergamon Press. 381 p.
103. Roussignol, P., et al., Time-Resolved Direct Observation of Auger Recombination in Semiconductor-Doped Glasses. *Applied Physics Letters*, 1987. **51**(23): p. 1882-1884.
104. Colombo, D.P., et al., Femtosecond Study of the Intensity Dependence of Electron-Hole Dynamics in Tio₂ Nanoclusters. *Chemical Physics Letters*, 1995. **232**(3): p. 207-214.
105. Ghanassi, M., et al., Time-Resolved Measurements of Carrier Recombination in Experimental Semiconductor-Doped Glasses - Confirmation of the Role of Auger Recombination. *Applied Physics Letters*, 1993. **62**(1): p. 78-80.
106. Potter, B.G., Electronic band structure and optical characteristics of quantum-size CdTe crystals in glass films, in *Materials Science and Engineering*. 1991, University of Florida: Gainesville, Florida. p. 217.
107. Potter, B.G. and J.H. Simmons, Quantum-confinement effects in CdTe-glass composite thin films produced using rf magnetron sputtering. *Journal of Applied Physics*, 1990. **68**(3): p. 1218-1224.
108. Potter, B.G. and J.H. Simmons, *Quantum confinement effects at the L point in CdTe*. *Physical review B*, 1991. **43**(3): p. 2234-2238.
109. Hecht, E., *Optics*. Third edition ed. 1998: Addison-Wiley.
110. SimmonsPotter, K. and J.H. Simmons, *Modeling of absorption data complicated by Fabry-Perot interference in germanosilicate thin-film waveguides*. *Journal of the Optical Society of America B-Optical Physics*, 1996. **13**(2): p. 268-272.
111. Malitson, I.H., *Interspecimen Comparison of Refractive Index of Fused Silica*. *Journal of the Optical Society of America*, 1965. **55**(10P1): p. 1205-&.
112. Sivfast, W.T., *Laser Fundamentals*. 1996: Cambridge University Press. 521.
113. Spectra-Physics, *Millenia Vs User's Manual*. 2000: Spectra-Physics.
114. Weber, M.J., *Handbook of Optical Materials*. 2002: CRC Press.
115. Rodney, W.S. and R.J. Spindler, *Index of Refraction of Fused-Quartz Glass for Ultraviolet, Visible, and Infrared Wavelengths*. *Journal of Research of the National Bureau of Standards*, 1954. **53**(3): p. 185-189.

116. Rodney, W.S. and R.J. Spindler, *Index of Refraction of Fused Quartz Glass for Ultraviolet, Visible, and Infrared Wavelengths: Errata*. Journal of the Optical Society of America, 1954. **44**(11): p. 889.
117. Potter, B.G., Electronic band structure and optical characteristics of quantum-size CdTe crystals in thin films, in Department of Materials Science and Engineering. 1991, University of Florida: Gainesville, FL.
118. Shoemaker, R.L., *Quantum optics class notes*. 2001.
119. Ochoa, O.R., et al., Quantum confinement effects on the photoluminescence spectra of CdTe nanocrystallites. Solid State Communications, 1996. **98**(8): p. 717-721.
120. Ochoa, O.R., et al., *Raman characterization of CdTe nanocrystallites embedded in a glass matrix*. Journal of Materials Science Letters, 1997. **16**(8): p. 613-616.
121. Ai, X.C., et al., *Femtosecond investigation of charge carrier dynamics in CdSe nanocluster films*. Journal of Chemical Physics, 1997. **106**(8): p. 3387-3392.
122. Mittleman, D.M., et al., Quantum-Size Dependence of Femtosecond Electronic Dephasing and Vibrational Dynamics in Cdse Nanocrystals. Physical Review B, 1994. **49**(20): p. 14435-14447.
123. Padilha, L.A., et al., *Recombination processes in CdTe quantum-dot-doped glasses*. Applied Physics Letters, 2004. **85**(15): p. 3256-3258.
124. Cruz, C.H.B., et al., *Ultrafast processes in semiconductor doped glasses*. Applied Surface Science, 1997. **110**: p. 30-35.